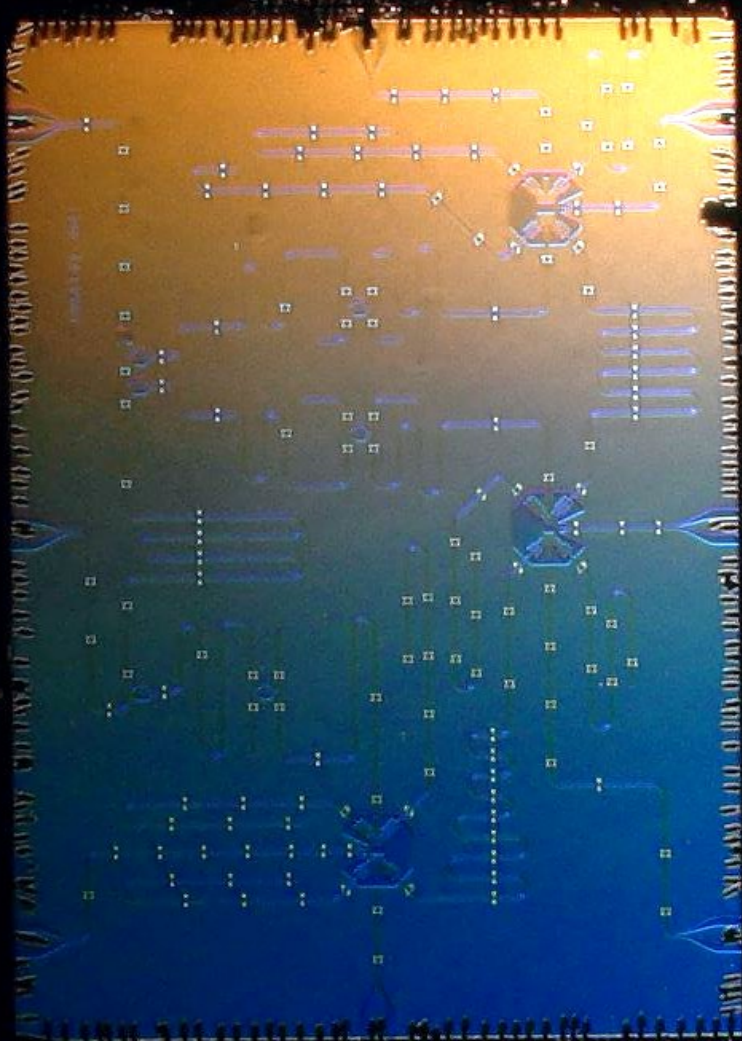René Vollmer

Fast and scalable readout for fault-tolerant quantum computing with superconducting Qubits

Fast and scalable readout for fault-tolerant quantum computing with superconducting Qubits

René Vollmer

Supervision:	Niels Bultink
	Leonardo Di Carlo
Defence Committee:	Menno Veldhorst
	Wolfgang Tittel
	Leonardo Di Carlo
	Niels Bultink

A thesis submitted in partial fulfilment of the requirements
for the degree of Master in Applied Physics
To be publicly defended on 17.07.2018

QuTech, Department of Quantum Nanoscience
Delft University of Technology
July 10th of 2018

Abstract

In this work, the addition of a filtering resonator to protect against Purcell decay in the surface code implementation presented in [1] is investigated. The requirements on single- and two-qubit gate operation as well as readout is outlined. We model the system with differential equations to optimize the coupling strengths and target frequencies for fast readout and minimized dephasing of untargeted qubits. The currently used qubit design is adapted to achieve these goals. A proof-of-concept chip, containing a subset of the surface code is implemented using these altered qubits, fabricated and characterized. On this device, state-of-the art readout fidelities of >98% within 450 ns are demonstrated. Back-action on untargeted qubits is measured and an upper bound is determined.

II

Contents

1   Motivation

The ultimate goal of quantum computation is to perform a range of computations that are very demanding on classical digital computational systems. Major speed-ups for many relevant algorithms have been shown and many more have been proposed. One example is the simulation of quantum systems itself [2]. For instance, the amount of continuous variables required to describe a multi-quantum-particle system scales exponentially with the number of particles. This means, that simulation of the time evolution of a quantum system takes exponential resources in a classical computer. On a device using (representative) quantum states, the same simulation has only polynomial complexity [3, 4]. Efficiently simulating quantum systems is an interesting and desirable goal in itself, but it also gives an intuitive understanding of the significant resources potential algorithms running on such a system could use. The most famous example of one such is probably Shor's algorithm, that can find the prime factors of an integer in a time that scales polynomially in the number of digits of the integer to be factored, while all known classical algorithms scale exponentially [5].

The building block of such a computer, a so called qubit, is a system that contains a quantum state that needs to be preserved (coherent) throughout the computation, but at the same time is accessible in order to perform gates and readout on it. More specifically, the time the state is preserved (life-time) should be much larger than the execution time of the operations (gates) required for a chosen algorithm (DiVincenzo's criteria [6]). Due to the fragile nature of quantum states, current life-times of physical and accessible quantum system are very limited. Therefore, it has been proposed to use an error-correction scheme [7] that can be executed over a system of such states to prolong the coherence time of the whole system. For such a quantum error correction (QEC) scheme, an overhead in the number of qubits is required. Using a special quantum property, entanglement, with a set of ancillary qubits, potential continuous errors can be discretised and detected through measurement of the ancillary qubits. Although the physical qubits decohere, the logical computational state prevails. Thus, it is often seen as paramount to provide a system which can perform error-correction algorithms to pave the path to quantum computation. For this, it is however required that each constituent qubit sufficiently fulfils the requirements to run this algorithm [8, 9]. As discussed before, a large number of readouts on ancillary qubits is required. One aspect of quantum measurements is their destructive nature: the measured continuous state will be reduced to a discrete value. Therefore, it is of essence to not accidentally measure the state of the logical qubit while reading out the ancillary qubit for QEC.

Many physical quantum-mechanical systems have been proposed and tested to procure these building blocks. For this work, we focus on an approach that utilizes circuit quantum electrodynamics (cQED) and more specifically *transmons*. Excitations of a resonant LC-circuit constitute the quantum state in a transmon. By coupling it to a number of microwave transmission lines allows individual manipulation, coupling to neighbouring qubits for two-qubit operations and readout [10]. However, due to this coupling, the qubit state can slowly leak into the resonant modes, limiting the lifetime. This so-called Purcell effect mostly concerns the readout resonator, since it is strongly coupled to both the qubit and the environment. In order to gain higher lifetimes

the qubit can be coupled more weakly, but this will also increase the time required for readout. This poses a problem for algorithms that rely on a high number of readouts, such as error-correction.

In order to allow faster readout while maintaining a reasonable life time, it has been investigated how the Purcell effect can be suppressed. Several solutions have been proposed and tested. One approach is the use of a tuneable coupling such that the readout resonator can be mostly decoupled from the environment during the qubit-resonator interaction [11]. Another solution is the implementation of an additional resonator, the Purcell filter, between the readout resonator and the environment to block leakage at the qubit frequency while being transparent for the readout resonator [12–15]. The implementations so far however, have not yet addressed aforementioned issue of unintended (partial) measurement of the logical qubit during QEC.

The goal of the DiCarlo group at the Technical University of Delft is to implement the seven-qubit surface code [16] on a single chip (often referred to as *S7 Chip*). Thus, we endeavour in this project to apply a Purcell filtering scheme to the seven-qubit surface chip. This entails optimizing the system's parameters with repetitive and parallel readout in mind.

2 Surface Code Error Correction with Superconducting Qubits

In the following sections a review of the surface code and the operating principles of the chosen elemental qubit, the transmon is given. Furthermore, the high-level design consideration and choices for the physical implementation of the surface code are discussed.

2.1 Introduction to the Surface Code

In the surface code, the computational state of one qubit is encoded into the joint state of several, so-called data qubits. These data qubits are interleaved with ancilla qubits. These ancilla qubits are used to extract onformation about decoherence events in the data qubits. This is done by performing parity measurements. Z-parity measurements extract whether the sum of excitations in the surrounding qubits is even or odd. Thereby, without direct measuring the data qubits (which would collapse all logical information) error events, can be discretized and extracted. Certain implementations of this scheme can protect against different kind of errors and enable the measurement outcomes to be used to localize and correct occurring errors [17].
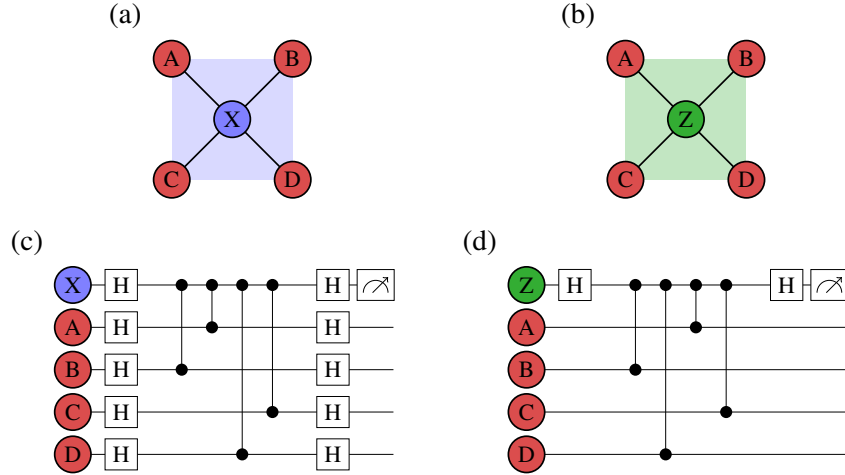

Figure 2.1: (a) X-type and (b) Z-type plauqettes. Circles represent qubits and the connecting lines connectivity for two-qubit gates. Example circuits using controlled-phase gates for measuring (c) X-type and (d) Z-type stabilizers indirectly using ancillas [1].

The parity measurements (stabilizers) are implemented by sequentially entangling four of the data qubits with the ancilla through two-qubit gates and consequent projective measurement of the latter [1]. Each of these ancillas, coupled to the nearest-neighbour data qubits, thus form a plaquette, see Fig. 2.1 (a,b). Examples of according error-detection circuits can be found in Fig. 2.1 (c,d). Using overlapping X- and Z-type plaquettes, a checkerboard lattice as in Fig. 2.2 can be constructed. This layout allows alternating execution of the two types of stabilizer measurements, where the gates can be executed in parallel with the ancilla measurement on the other plaquettes.

Finally, it should be noted that the efficiency of this algorithm depends on the accuracy and speed with which each of the operations can be performed. If more errors are introduced due to inaccurate gates or incorrect parity measurement results, the surface code can even have a negative impact on the coherence time of the logical state. Numerical analysis [18], shows that all operations

must have an accuracy better than roughly 10^{-3}. Furthermore, with currently achievable transmon coherence times of approximately $80\,\mu$s, single-qubit gates should not take longer than $20\,$ns, two-qubit gates $40\,$ns and readout $100\,$ns. While gate operation very close to that goal has been demonstrated, readout currently requires approximately $400\,$ns.

2.2 Basic Transmon

Here, we review implementation and operation of the chosen building block of the surface code, the transmon. An inductor in parallel with a capacitor constitutes a harmonic oscillator. When this cicuit is implemented at microscopic scale using superconducting components and low-loss dielectrics, narrow quantized levels occur at low temperatures. In the following, the levels are referred to by number; $|0\rangle$ for the ground, $|1\rangle$ for the first and $|2\rangle$ for the second excited state. Using a Josephson junction (JJ), which exhibits an inductance linear instead of constant in current, deforms the harmonic potential and thus lifts the degeneracy of the level splittings. This anharmonicity is crucial, because it yields selective addressability of the $|0\rangle \leftrightarrow |1\rangle$ transition from transitions to higher states, which allows using the transmon as a qubit. In this research, $|0\rangle$ and $|1\rangle$ are used as the computational states and transitions to higher states are considered as leakage out of this subspace.
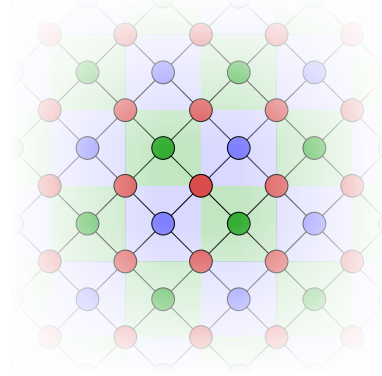

Figure 2.2: X- (blue) and Z-type (green) plaquettes, as in Fig. 2.1 (a,b), arranged in a checkerboard lattice to form the surface code hardware.

The JJ energy E_J of a single junction is $E_J^1 = I_0\Phi_0$, where $\Phi_0 = \hbar/2e$ is the flux quantum, $\hbar$ the reduced Planck constant and I_0 the critical current of the junction. Together with the charging energy of the capacitor, $E_C = e^2/2C$, where C is the capacitance between the two sides of the circuit, it defines the potential and thus qubit frequency and anharmonicity [19], as illustrated in Fig. 2.3 (a). In this work, we implement the qubit with a high ratio of $E_J/E_C > 40$, since a drastically lower sensitivity to charge noise can be observed in this regime. The transition energy from ground to first excited state of the system can then be estimated as [10]

$$E_{01} \simeq \sqrt{8E_J E_C} - E_C \ ,$$

where E_{ij} is the transition energy between state $|i\rangle$ and $|j\rangle$ and $\omega_{ij} = E_{ij}/h$ the angular frequency associated with the transition, where h is the Planck constant. The anharmonicity $\delta_\alpha := E_{12} - E_{01}/h$ is found to be $\delta_\alpha \simeq -E_C/h$.

Two JJs in parallel enclosing an area form a superconducting quantum interference device (SQUID) [20]. In contrast to the single JJ with a constant E_J, the SQUIDs effective E_J is dependent on the magnetic flux Φ through the enclosed area [21]

$$E_J = E_{J,\text{max}} \cdot |\cos(\Phi/\Phi_0)| \ ,$$

where $E_{J,\max}$ is the combined JJ energy of the double-junction at zero flux. The derivative of this energy becomes zero at certain flux values. Consequentially, the qubits frequency is first-order insensitive to flux noise at this point. Therefore, longer coherence times can be expected when the qubit is at that frequency. Note that at these points of insensitivity, the associated qubit frequency has a maximum and are often referred to as sweetspots. This circuit, see Fig. 2.3, is often implemented with two coplanar pads (often called islands) which form the capacitor, connected by the JJs. In its first implementation, this type of qubit was referred to as transmission-line shunted plasma oscillation qubit (transmon) [10].
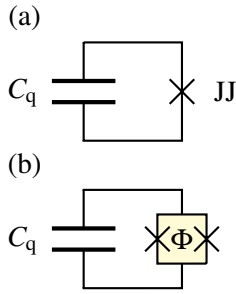
2.3 Transmon Gates

(a)

(b)

Figure 2.3: Circuit representation of a transmon with (a) a single JJ and (b) a SQUID enclosing flux Φ as non-linear inductive element.

By resonantly driving a transmon with ω_{01}, the qubit can be rotated along along arbitrary axis in the xy-plane, depending on the phase of drive w.r.t. the Larmor precession of the qubit. This is commonly implemented by coupling a so-called driveline to the qubit, where the exact magnitude of the coupling is not very important, because it can easily be compensated with the amplitude of the drive pulse. For short gate times (on the order of tens of nanoseconds, which are often desirable), the Fourier-spectrum becomes rather wide as seen in Fig. 2.4. The pulse is thus weakly driving the detuned $|1\rangle \leftrightarrow |2\rangle$ transition, which takes the Qubit out of the computational subspace. Convolution with or the use of Gaussian shapes can greatly reduce this effect, as compared in Fig. 2.4. Remaining leakage can be eliminated further by adding a derivative-of-Gaussian component to the pulse [22].
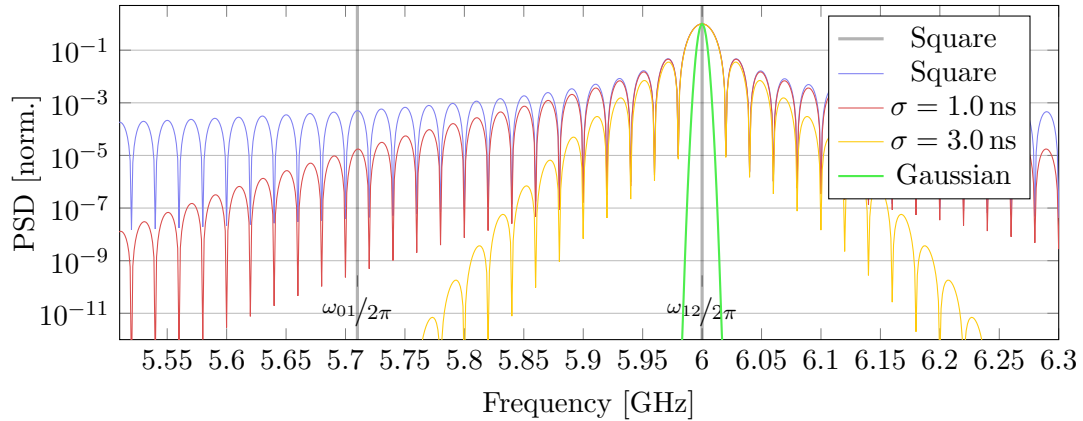
Figure 2.4: Power Spectral Density (PSD) of a 50 ns square pulse modulated at 6 Ghz and of the same pulse, softened by convolution with a Gaussian of width σ as well as a pure Gaussian pulse with $\sigma = 50$ ns. Marked are typical examples of qubit state transition frequencies. Clearly, the convolution reduces the PSD at the transition frequency of the second excited state.

Controlled or multi-qubit gates require interaction between the Qubits. In transmons, this is realized through pairwise off-resonant (dispersive) coupling of the according two Qubits to a bus resonator. This allows for a conditional-phase (CZ) by bringing the $|1\rangle \leftrightarrow |2\rangle$ transition of the

5

target into resonance with the $|0\rangle \leftrightarrow |1\rangle$ transition of the control qubit. In other words, if Qubits 1 and 2 with $\omega_{\text{int}} = \omega_{01}^1 = \omega_{12}^2$, where $\omega_{jk}^i = E_{jk}/h$ of Qubit i, couple with strength g_1 and g_2 to a shared bus resonator with frequency ω_{b} the interaction strength is approximately [23]

$$J_2 \simeq \sqrt{2} \cdot J_1 = \frac{\sqrt{2} \cdot g_1 \cdot g_2}{\omega_{\text{int}} - \omega_{\text{b}}} \quad . \tag{2.1}$$

In order to perform an CZ gate in 50 ns, an interaction rate of $J_1/2\pi = 14\,\text{MHz}$ is required. Since adiabatic gate operation will increase the gate time, a higher coupling of $J_1/2\pi = 15\,\text{MHz}$ is targeted.

2.4 Transmon Readout Theory

For readout, the transmon is dispersively coupled to a harmonic mode [24]. This can for instance be done by capacitive coupling to a resonator as in Fig. 2.5 (a). The Hamiltonian of such a system can be approximated as [10]

$$\hat{H}_{\text{eff}} = \frac{\hbar \omega_{\text{q}}}{2} \hat{\sigma}_{\text{z}} + (\hbar \omega_{\text{r}} + \hbar \chi \hat{\sigma}_{\text{z}}) \hat{a}^\dagger \hat{a} \quad ,$$

where $\omega_{\text{q}} = \omega_{01}$ is the qubit and ω_{r} the resonators frequency, χ the dispersive shift, $\hat{a}$ $(\hat{a}^\dagger)$ the resonator photon annihilation (creation) and σ_{z} the projection operator. The second term of the Hamiltonian clearly shows, that the frequency of the readout resonator's (RR) photon population is dependent on the qubit state. The frequency shift associated with the state, the so called dispersive frequency shift, can be expressed as [24]

$$\chi \simeq \frac{g^2}{\Delta} \frac{\delta_\alpha}{\delta_\alpha + \Delta} \quad , \tag{2.2}$$

with $\Delta = \omega_{\text{q}} - \omega_{\text{r}}$, the coupling strength g and the anharmonicity δ_α of the qubit. If a RR is coupled to a transmission line, the feedline, its resonance frequency can be probed and thus the qubit state be determined. It appears natural to increase the coupling g as far as possible in order to increase the signal and speed up the readout process. Unfortunately, quantum systems decohere into connected resonant modes: the rate of this so-called Purcell-effect Γ_{P} depends on the coupling strength [25]

$$\Gamma_{\text{P}} \simeq \kappa_{\text{r}} \left(\frac{g}{\Delta} \right)^2 \quad . \tag{2.3}$$

It can be seen from this formula, that reducing the coupling κ_{r} towards the feedline would reduce Γ_{P} again. Unfortunately, that entails an increase in ring-up and -down time, effectively limiting the readout time t_{m} ideally to $t_{\text{m}} \geq 4\kappa_{\text{r}}^{-1}$ or under most realistic circumstances even $t_{\text{m}} \gg 10\kappa_{\text{r}}^{-1}$ [26].

An elegant solution to solve this dilemma is the use of a Purcell filter (PF), an additional resonator connecting the readout resonator and feedline, see Fig. 2.5 (b), that suppresses transmission at the qubit frequency, while almost fully transmitting the readout photons [12, 13]. Consequentially, the bandwidth of the PF, κ_{f} that is relevant for the accumulation and depletion of photons in the RR is different from the κ_{r} in Eq. (2.3). More concretely, the transmission of a resonator at a frequency ω_{d} far from resonance ω_{r} is proportional to $1/\Delta_{\text{dr}}^2$, where $\Delta_{\text{dr}} = \omega_{\text{d}} - \omega_{\text{r}}$, while in the double-resonator case it is proportional to $1/\Delta_{\text{dr}}^4$. As a result, a much higher suppression for photons
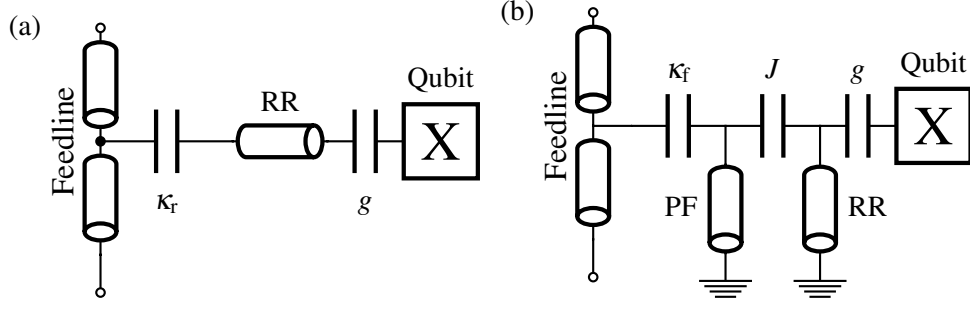
6

Figure 2.5: (a) Schematic of a regular single-qubit readout set-up. In this case a half-wave readout resonator (RR) and capacitive coupling was chosen. (b) Schematic of a Purcell-filtered single-qubit readout set-up. Here, both the RR and PF were chosen as $\lambda/4$ resonators and all couplings are capacitive.

at the qubit frequency can be expected [27].

Through various means like classical circuit or quantum analysis, the Purcell rate for this filtered system can be found to be [26]

$$\Gamma_P = \frac{g^2 |J|^2 \kappa_f}{\Delta^2 \left[\left(\Delta_{fq} - |J|^2/\Delta\right)^2 + (\kappa_f/2)^2\right]} \approx \kappa_q \left(\frac{g}{\Delta}\right)^2 \quad , \tag{2.4}$$

with $\Delta_{fq} = \omega_f - \omega_q$ the detuning between qubit and PF with frequency ω_f, J the coupling between RR and PF and

$$\kappa_q = \frac{4 |J|^2}{\kappa_f} \frac{1}{1 + [2\Delta_{fq}/\kappa_f]^2} \quad .$$

This is the κ relevant for the Purcell decay, while

$$\kappa_r = \frac{4 |J|^2}{\kappa_f} \frac{1}{1 + [2\Delta/\kappa_f]^2} \tag{2.5}$$

the κ determining the readout. This directly leads to the relation $\kappa_q/\kappa_r \ll 1$, which promises a highly reduced Purcell loss channel without hindering the readout [27].

2.5 Frequency Layout in the Surface Code

For many quantum algorithms and certainly for the surface code, it is required to be able to target specific qubits with a particular action. For instance, ancilla qubits are read-out during error-correction, while the data qubits should not be influenced. For single-qubit gates, this can be achieved by means of dedicated lines, that couple to only one qubit. For two-qubit gates and readout, addressing is done in frequency space. Here, we review the scheme to distribute the resonators and qubits in frequency space as presented in [1].

The interaction for two-qubit gates can be facilitated or suppressed by bringing the according transitions into or out of resonance. Commonly, the lower of the two sweetspot frequencies of the involved qubits is used as interaction frequency. The interaction cannot occur at higher frequencies, because of the fact that the sweetspot constitutes the highest possible frequency. Choosing a lower frequency on the other hand, would just move both qubits further away from their (flux-noise

resistant) sweetspot.

With the lattice of qubits with nearest-neighbour interaction, an efficient scheme for the selective execution of two-qubit gates need to be in place. This process should aim for two goals: enabling parallel execution of gates for the stabilizer measurements and maximal use of the flux-noise protection at their respective sweetspots. The simplest possible scheme would only use two frequencies for the qubits: one for all data and one for all ancialla qubits. For the presented goals, both choices for the lower frequency are the same. Defining the data qubits frequency as the higher of the two, the ancillas need to be lower in frequency by the anharmonicity with an additional margin to disable the interaction when both qubits at their sweetspots. The data qubits can remain at their sweetspot when not involved in a controlled gate.

Figure 2.6: Surface code lattice with marked high (H), low (L) and mid (X and Z ancilla) qubits.

Unfortunately, this is not true for the ancillas: they need to be tuned down from their sweetspot when any of the neighbouring qubits is involved in any controlled gate to avoid unwanted interaction. In that time they cannot interact with any of the data qubits, increasing the total execution time of the stabilizers. If every second data qubit in a row of ancillas is however replaced by a qubit that operates at a frequency below the ancillas, the ancillas previously not able to interact, can perform gates with the lower data qubits. Using three types of qubits (QL, QM, QH in ascending order of frequency) with the frequency arrangement as in Fig. 2.7, also allows the data qubits to remain at their sweetspots for most of the error correction cycle.

To summarize, this scheme uses three types of qubits (QL, QM, QH in ascending order of frequency) with different sweetspot frequencies in a pattern as seen in Fig. 2.6, where the colours of the circle indicate the three different frequencies. When interleaving the two types of stabilizers where the gates on one overlap with the ancilla qubit measurement of the other, this allows for a very high degree of parallelisation. Furthermore we note, that this scheme is fully scalable, where eight qubits form one unit cell.

The scheme as presented above requires the ability to tune each qubits frequency. As described in Sec. 2.2, this tunability can be achieved by changing the magnetic flux through the SQUID-loop. The scheme does however require us to independently control this flux. A common solution is to have current, supplied by a dedicated connection for each qubit, produce a magnetic field near each SQUID. By means of varying the current, the local magnetic field and thus the qubits frequency can be changed. These lines are often referred to as fluxlines.

Another requirement is the fast and targeted readout of each qubit. It is desirable to minimize the amount of transmission lines into and out of the device. Furthermore, high fidelity readout
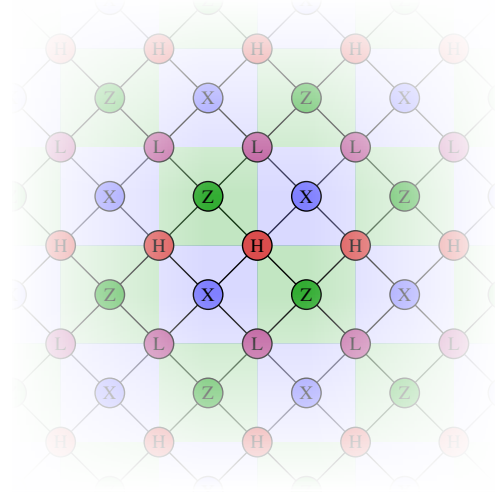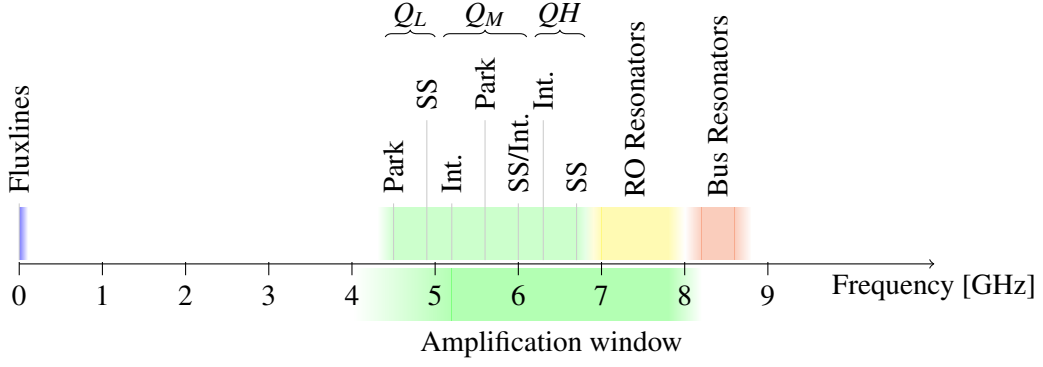
Figure 2.7: Frequency layout of the elements in the surface code as proposed here.

requires a rather complex amplification chain, making it desirable to use each for several qubits. Thus several qubits are coupled to the same feedline at different frequencies. By choosing the probe signals frequency, targeted readout of a certain qubit can be accomplished. Frequency multiplexing (using a multi-tone signal) allows for parallel readout. However, reading out the ancillas during the error-correction-cycle should not influence (i.e. dephase) the data qubits. Similar to the signals on the direct drive (see section 2.3), the spectral width of the readout signal can cause crosstalk. This is intensified by the fact that only a small window between roughly 7 and 8 GHz can be used to place readout resonators, limited by the qubit frequencies and the range, in which the signal processing chain shows sufficient amplification for fast, high fidelity readout. Investigation and reduction of this crosstalk is one of the goals of this work.

Above, we left open the choice of two-qubit coupling-bus frequencies. We note, that each qubit is connected to four busses, so as to avoid next-nearest neighbour-coupling, four distinct frequencies per Qubit with spacing $\Delta\omega_b$ should be chosen, that are additionally different from the readout-resonator. Since a higher coupling between busses connected to the same island is expected, such busses should be spaced by $2\Delta\omega_b$. Furthermore, the signals from the busses do not need to be amplified, so we can chose them to be above or below the amplification window and readout-resonator frequencies. To avoid having second harmonics of the busses at qubit or RR frequencies, we chose to place them above the RR, rather than below the qubits, so we assign the band from $8 - 9$ GHz for the busses.

3 Investigation of Photon Fields

In order to make predictions about the achievable readout speed and fidelity for certain properties of the readout system, we next set out to describe the readout process by a simple differential equation for the photon field derived from the master equation of the system [28].

3.1 Differential equations and Green's functions

For a single resonator dispersively coupled to a qubit as in Fig. 2.5 (a), the state dependent photon field $\alpha^{0/1}$ in the resonator can, in the rotating frame of the drive frequency ω_d, be described as [29, 30]

$$\dot{\alpha}^{0/1} = -i(\Delta_{rd} \pm \chi)\alpha^{0/1} - \kappa/2 \cdot \alpha^{0/1} - i\varepsilon \ ,$$

where $\dot{\alpha}^{0/1}$ denotes the first time derivative of $\alpha^{0/1}$, ε_r the drive amplitude, $\Delta_{rd} = \omega_r - \omega_d$ with ω_r the readout resonators angular frequency and the signs for the dispersive shift are associated with the ground $|0\rangle$ and excited $|1\rangle$ states accordingly. For this system it is easy to find an according Green's functions

$$G^{0/1}(t) = -j \cdot e^{-(j \cdot (\Delta_{rd} \pm \chi) + \kappa/2) \cdot t} \ .$$

This analytical solution allows to compute the photon field in the resonator depending on the incident readout pulse and the (projected) qubit state, which can be translated into the amount of acquired information (see section 3.2) and thus into the required readout time.

This approach can also be applied to the Purcell-filtered case. For a circuit as in Fig. 2.5 (b), where we associate $\alpha^{0/1}$ with the photon field in the readout resonator and $\beta^{0/1}$ in the Purcell filter, the equations of motion become [26]

$$\dot{\alpha}^{0/1} = -i(\Delta_{rd} \pm \chi)\alpha^{0/1} - iJ\beta^{0/1} \quad \text{and} \tag{3.1}$$

$$\dot{\beta}^{0/1} = -i\Delta_{fd}\beta^{0/1} - iJ^*\alpha^{0/1} - \kappa_f/2 \cdot \beta^{0/1} - i\varepsilon_f \ , \tag{3.2}$$

where $\Delta_{fd} = \omega_f - \omega_d$ with ω_f the Purcell filters angular frequency, J the coupling between the resonators and κ_f the decay rate of the Purcell filter. This system of differential equations can again be analytically solved to find the Green's functions

$$G_\alpha^{0/1}(t) = \frac{-J \cdot I_1^{0/1}(t)}{s} \quad \text{and}$$

$$G_\beta^{0/1}(t) = \frac{1}{s} \left[\Delta_a^{0/1} \cdot I_1^{0/1}(t) - I_2^{0/1}(t) \right]$$

with

$$I_1^{0/1}(t) = \exp(-i\omega_+^{0/1}t) - \exp(-i\omega_-^{0/1}t) \ ,$$

$$I_2^{0/1}(t) = \omega_+^{0/1} \cdot \exp(-i\omega_+^{0/1}t) - \omega_-^{0/1} \cdot \exp(-i\omega_-^{0/1}t) \ ,$$

$$\omega_\pm^{0/1} = \frac{1}{2}\left(\Delta_a^{0/1} + \Delta_b \pm s\right) \ , \quad s = \sqrt{(\Delta_a^{0/1} - \Delta_b)^2 - 4|J|^2} \ ,$$

$$\Delta_a^{0/1} = \Delta_{\text{rd}} \pm \chi \quad \text{and} \quad \Delta_b = \Delta_{\text{fd}} - i \cdot \kappa_f/2 \ .$$

It should be noted, that an input capacitor with capacitance C_{in} can be added behind the input port of the feedline. This causes a larger part of the photons to leave through the output port, instead of equally through input and output, doubling the readout efficiency. However, investigation of the input-output relations reveals, that the parameters κ_f and ω_f in differential equations (3.1) and (3.2) change slightly [31, App. C]

$$\kappa_f \to \kappa_f \frac{1 + \Re(\Gamma(\omega))}{2}$$
$$\omega_f \to \omega_f + \kappa_f \frac{1 + \Im(\Gamma(\omega))}{4} \ ,$$

where $\Gamma(\omega) = (1 + 2j\omega Z_0 C_{\text{in}})^{-1}$.

3.2 SNR, dephasing and active depletion calculations

The photon field itself does not allow for optimization of the parameters. For this, conversion into useful quantities, such as achievable readout fidelity or dephasing, needs to be performed. The following calculations can be used in either case: direct and Purcell-filtered readout, using the parameters as indicated in Tab. 3.1.

Table 3.1: Applicable parameters for the calculations in this section, depending on the readout topology.

	This section	**Direct readout**	**Purcell**
Relevant Photon field	$\alpha^{0/1}$	$\alpha^{0/1}$	$\beta^{0/1}$
Relevant Decay rate	κ	κ	κ_f
Drive	ε	ε_r	ε_f

The state-dependent photon field leaving the system after being driven with a certain readout pulse ε can be dissected into the real, in-phase (I) and imaginary, in-quadrature (Q) components that would be detected by the measurement electronics as [30, 32]

$$V_I^{0/1}(t) = V_0\left(\sqrt{2\kappa\eta} \cdot \Re(\alpha^{0/1}(t)) + n_I(t)\right) \tag{3.3}$$

$$V_Q^{0/1}(t) = V_0\left(\sqrt{2\kappa\eta} \cdot \Im(\alpha^{0/1}(t)) + n_Q(t)\right) \ , \tag{3.4}$$

where η is the efficiency of the measurement process, V_0 is an irrelevant scale factor, $\Re$ and $\Im$ denote the imaginary and real part, respectively, and n_I and n_Q are continuous, independent Gaussian white noise terms with unit variance

$$\langle n_j(t) \cdot n_k(t')\rangle = \delta_{j,k} \cdot \delta(t - t') \ . \tag{3.5}$$

The most direct way to obtain a signal used to differentiate between the two states is comparison of the integrated components. The signal-to-noise ratio (SNR) can however be increased by weighting the measured voltages according to its amplitude relative to the noise. For this, the functions $W_I(t)$

and $W_Q(t)$ are introduced and the integrated voltage then becomes

$$V_{\text{int}}^{0/1} = \int V_I^{0/1}(t)W_I(t) + V_Q^{0/1}(t)W_Q(t)\, dt \ ,$$

The signal is then the absolute separation between the averaged weighted and integrated voltages $S = \langle \Delta V_{\text{int}} \rangle$ with $\Delta V_{\text{int}} = V_{\text{int}}^1 - V_{\text{int}}^0$. Using Eqs. (3.3) and (3.4), we can rewrite

$$\Delta V_{\text{int}} = V_0\sqrt{2\kappa\eta}\int W_I(t)\cdot\Re(\alpha^1(t) - \alpha^0(t)) + W_Q(t)\cdot\Im(\alpha^1(t) - \alpha^0(t))\, dt$$

$$+ V_0\int W_I(t)n_I(t)W_Q(t)n_Q(t)\, dt - V_0\int W_I(\tilde{t})n_I(\tilde{t})W_Q(\tilde{t})n_Q(\tilde{t})\, d\tilde{t} \ ,$$

which allows us, due to the property (3.5) of the noise-terms, to express the signal as

$$S = 2\kappa V_0^2 \left\langle \int G_{I(t)}\cdot\Re(\alpha^1(t) - \alpha^0(t)) + W_Q(t)\cdot\Im(\alpha^1(t) - \alpha^0(t))\, dt \right\rangle \ .$$

The measured noise is defined as the standard deviation of the signal

$$N = \sqrt{\langle(\Delta V_{\text{int}} - \langle \Delta V_{\text{int}}\rangle)^2\rangle}$$

$$N^2 = V_0^2 \left\langle \int W_I^2(t)n_I^2(t) + W_Q^2(t)n_Q^2(t) - W_I(t)W_Q(t)n_I(t)n_Q(t)\, dt \right\rangle$$

$$= V_0^2 \left\langle \int W_I^2(t) + W_Q^2(t)\, dt \right\rangle$$

Putting the measured signal and noise terms together, one obtains the SNR as

$$\text{SNR} = \frac{S}{N} = \frac{2\kappa\eta \left\langle \int W_I(t)\cdot\Re(\alpha^1(t) - \alpha^0(t)) + W_Q(t)\cdot\Im(\alpha^1(t) - \alpha^0(t))\, dt \right\rangle}{\sqrt{\left\langle \int W_I^2(t) + W_Q^2(t)\, dt \right\rangle}} \ .$$

Using the optimal weight functions, which are given by the average of the difference of the field components [33, 34]

$$W_x = \langle V_x^1 - V_x^0 \rangle \ , \tag{3.6}$$

the SNR can simply be expressed as

$$\text{SNR} = 2\kappa\eta\sqrt{\left\langle \int |\alpha^1(t) - \alpha^0(t)|^2\, dt \right\rangle} \ . \tag{3.7}$$

Furthermore, the SNR can then easily be related to the expected assignment fidelity by

$$F = 1 - \text{erfc}\left(\tfrac{SNR}{2\sqrt{2}}\right)/2 \ .$$

Analogously, it can be used to calculate the measurement-induced dephasing due to the drive

signal. The coherence elements of the qubit density matrix are reduced as [30]

$$|\rho_{01}(t=T)| = e^{-\gamma_m} |\rho_{01}(t=0)| \quad , \text{with} \tag{3.8}$$

$$\gamma_m = 2\chi \int_0^T \Im\left(\alpha^0(t)\bar{\alpha}^1(t)\right) \, dt \quad . \tag{3.9}$$

Furthermore, it is possible to use the found Green's function to calculate a drive-pulse, based on the photon population at any point, that actively depletes the resonator. This active depletion thus reduces the ring-down time in the resonator and can as a consequence potentially reduce the overall readout time [32].

3.3 Verification with CST

In order to verify the applicability of the obtained differential equations, simulations in the commercial microwave simulation software *CST Design Studio* were attempted. As a model, a circuit as in Fig. 3.1 was implemented in CST. To emulate the effect of the qubit, the resonance frequency of the readout resonator has been shifted by the anticipated value 2χ.
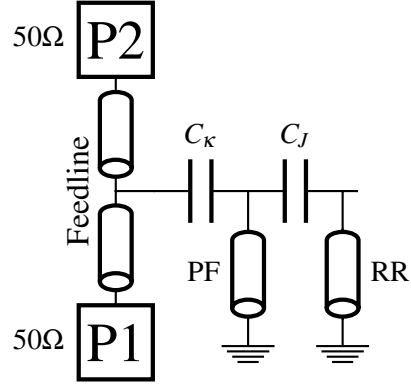

Figure 3.1: Simplified schematic of a Purcell-filtered single qubit readout set-up for simulation with microwave software. P1 and P2 are $50\,\Omega$ ports which have been used to insert the readout pulse and extract the scattering matrix. Here, both the readout-resonator (RR) and the Purcell-Filter (PF) are $\lambda/4$ resonators.

Next, a file containing time-domain samples of the desired readout pulse has been generated and loaded into CST and defined as a current source at Port 1. A voltage probe has been placed at the junction of C_κ and PF. Then, time-domain simulations were conducted. The probe recorded the simulated voltage over the simulation. For further processing, translation into the I and Q components in the rotating frame had to be conducted, see Ch. 3.2. For this, the extracted signal was multiplied with the sine and cosine at the drive frequency respectively and then lowpass-filtered.

Additionally, CST can extract the frequency dependent scattering matrix S, whose entries represent the reflection and transmission at steady-state between the ports 1 and 2 [35]. Solving Eqs. 3.1 and 3.2 for steady-state $\dot{\alpha} = \dot{\beta} = 0$, results in

$$\frac{\alpha}{\varepsilon} = -\frac{j\sqrt{\kappa}\Delta_{rd}}{J^2 + j\Delta_{fd}\left[\kappa + 2j\Delta_{rd}\right]} \quad .$$

For the transmission of the coupled feedline, this results in

$$|S_{21}(\omega)| = A\left|1 + \sqrt{\kappa}\cdot\frac{\alpha}{\varepsilon}\right| = A\left|1 - \frac{j\kappa(\omega - \omega_r)}{J^2 + j(\omega - \omega_r)\left[\kappa + 2j(\omega - \omega_f)\right]}\right| \quad , \tag{3.10}$$

where the dispersive shift has been absorbed into the resonator's frequency and *A* is an irrelevant amplitude set by the input-output relations for the system. Consequently, by fitting this function to the simulated scattering matrix entry, the effective parameters for the differential equation approach can be extracted. Inserting these values and using the same drive-pulse, the resulting photon field trajectories were be compared, for which a very good visual correlation was found.

4 Circuit Quantum Electro-Dynamics

In circuit quantum electrodynamics (cQED), coupled resonator systems play a major role. In many cases a precise frequency and bandwidth targeting is required. The following sections thus show calculations and methods to determine the physical layouts required to obtain certain parameters.

4.1 Coplanar Waveguides

The fundamental building block in cQED [24] of each transmission line (TL) or resonator are coplanar waveguides (CPWs). Waveguides are the preferred TL for cQED due to their low loss and high power capacity [35].They consist of a central conductor of width w. separated from the ground plane on each side by a gap of s. Each unit-length segment of this TL can be represented as a parallel capacitive element and a series inductive element, see Fig. 4.1 [35].
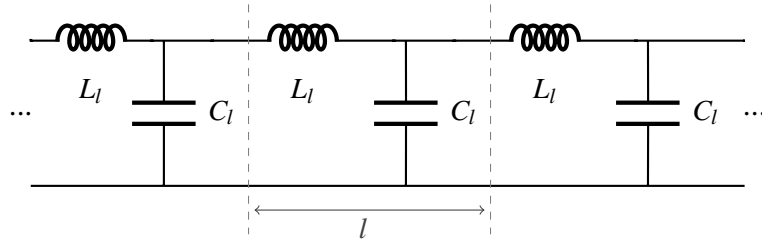

Figure 4.1: Lumped-Element representation of a transmission line with unit cells of length l with inductance L_l and capacity C_l.

The capacitances C_l and inductances L_l per unit length can generally be estimated from geometric considerations as [36]

$$L_l \simeq L_l^{(g)} = \frac{\mu_0}{4} \frac{K(k_0')}{K(k_0)} \qquad \text{and} \qquad C_l = 4\varepsilon_0 \varepsilon_{\text{eff}} \frac{K(k_0)}{K(k_0')} \quad ,$$

where K denotes the complete elliptic integral of the first kind, their parameters are defined as

$$k_0 = \frac{w}{w+2s} \qquad \text{and} \qquad k_0' = \sqrt{1-k_0^2}$$

and ε_{eff} is the effective electric permittivity of the substrate, depending on its permittivity and the CPW's geometry. It is often considered more accurate to use finite-element simulations to determine the capacity C_l directly, rather than calculating ε_{eff} [37]. An example of ε_{eff} and results of such a simulation for our substrate can be found in App. A.

Due to the superconductivity of films in cQED however, additionally kinetic inductance needs to be taken into account. This can be found by analytical considerations for $2\lambda > t$ as

$$L_l^{(k)} = \mu_0 \frac{\lambda^2}{tw} g(s,w,t)$$

$$g(s,w,t) = \frac{1}{2k_0^2 \cdot K(k_0)^2} \left[-\ln\left(\frac{t}{4w}\right) - k_0 \ln\left(\frac{t \cdot k_0}{4}\right) + \frac{2(w+s)}{w+2s} \ln\left(\frac{s}{w+s}\right) \right] \quad ,$$

where t is the thickness and λ the magnetic penetration depth of the conductor [38]. It should be

noted that the kinectic inductance can be found from just the geometrical parameters and penetration depth. The latter can be estimated for temperatures below the critical temperature of the conductor, T_C, from measurement of the resistivity $\rho(T_C)$ by using the expression [38]

$$\lambda \simeq \lambda(0) = 1.05 \times 10^{-3} \sqrt{\rho(T_C)/T_C} \cdot \sqrt{\mathrm{K\ m}/\Omega} \ .$$

The inductance per unit length is then $L_l = L_l^{(\mathrm{g})} + L_l^{(\mathrm{k})}$.

4.2 Coupled Resonators

Resonators can be constructed by imposing boundary conditions on a TL that restrict propagation of the wave and thus produce standing waves. The length of these is dependent on these boundary conditions and thus determine the resonance frequency ω and the rate at which energy leaves the resonator. Any resonant system with an power leakage has a finite linewidth. This resonance width or full width at half maximum (FWHM) $\Delta\omega$ is

$$\Delta\omega = \frac{\text{power leaving system}}{\text{energy stored in resonator}} \tag{4.1}$$

and the dimensionless quality factor of a resonator is defined as

$$Q := \frac{\omega}{\Delta\omega} \ .$$

Obviously, there are different ways in which power can leave the resonator system. Generally, internal loss, which include resistive, radiative and dielectric dissipation, and energy lost due to coupling are distinguished. Thus, the total bandwidth can be found by adding all power loss channels of the system together

$$\Delta\omega = \frac{\sum_i P_i}{E} = \sum_i \frac{P_i}{E} = \sum_i \frac{\omega}{Q_i} \ ,$$

where E is the energy stored in the resonator, the P_i's are the different power loss channels and Q_i are the associated quality factors. Often, the coupling strength is expressed as the partial bandwidth, for instance $g = \frac{\omega}{Q_C}$.

For CPWs, these boundary conditions are usually constituted by either inductive or capacitive elements. The simplest imaginable such system would be a lossless quarter-wavelength TL with characteristic impedance Z_l, shorted on one end and capacitively coupled to Z_0 on the other end, as seen in Fig. 4.2 (a). The energy stored in a capacitor of capacitance C with a voltage V across it is equivalent to $CV^2/2$. Thus, using the lumped-element model of the TL, the energy stored in the capacitive part is $E_C = LC_l \langle V^2 \rangle/4$, where another factor of $1/2$ was introduced due to the averaging of the voltage over one cycle of the oscillation and D is the total length of the TL. Due to the fact that

18

$E_C = E_L$, the total stored energy is

$$E = 2E_C = \frac{1}{2}LC_1\langle V^2\rangle \ . \tag{4.2}$$

The power leaving the system through the capacitor can be described as $P_C = 2\langle I^2\rangle Z_0$. Assuming
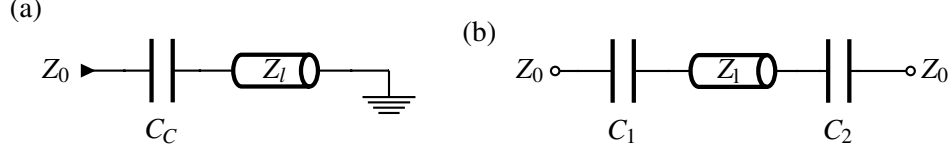

Figure 4.2: (a) A quarter-wavelength TL, shorted on one end and capacitive coupling to a Z_0 environment on the other. (b) A half-wavelength TL, capacitively coupled to Z_0 environments on both ends.

the dominance of the coupling capacitance C_C over the impedance, the current through the capacitor is $I = C\frac{\partial V}{\partial t} = C\omega V(t)$, where ω_r is the resonance frequency of the coupled resonator. Thus, the power leaving the TL is

$$P_C \simeq 2\langle(\omega_r C_C V)^2\rangle Z_0 = 2\omega_r^2 C_C^2\langle V^2\rangle Z_0 = -2\langle V^2\rangle Z_0/Z_C^2(\omega_r) \ , \tag{4.3}$$

where $Z_C(\omega) = -j/\omega C_C$ is the complex impedance of the capacitor. Rewriting

$$DC_1 = D\frac{\sqrt{L_1 C_1}}{\sqrt{D_1/C_1}} = \frac{D}{Z_1 v} = \frac{\pi}{2\omega_0 Z_1} \ ,$$

using that $D = \frac{\lambda}{4} = \frac{2\pi}{4\omega_0}$ with ω_0 the uncoupled resonator frequency, and bringing this result together with Eqs. (4.1), (4.2) and (4.3), the coupling strength is

$$g = \frac{P_C}{E} \simeq \frac{2\omega_r^2 C_C^2\langle V^2\rangle Z_0}{\frac{1}{2}LC_1\langle V^2\rangle} = \frac{2\omega_r^2 C_C^2\omega_0 Z_0 Z_1}{\pi} = -\frac{2\omega_0 Z_0 Z_1}{Z_C^2(\omega_r)\pi} \ . \tag{4.4}$$

Similar considerations can be done for other systems, such as a lossless half-wave TL with capacitor C_1 on one and C_2 on the other (Fig. 4.2 (b)), which leads to the result [39]

$$g \simeq \frac{4\omega_0\omega_r^2(C_1^2 + C_2^2)Z_0 Z_1}{\pi}$$

$$= -\frac{4\omega_0 Z_0 Z_1}{\pi\left[Z_{C_1}^2(\omega_r) + Z_{C_2}^2(\omega_r)\right]} \ .$$

Also, there are non-capacitive (purely inductive) or mixed couplings possible. The expression for these couplings can be generalized to

$$g \simeq -\frac{8\omega Z_0 Z_1}{m\pi\left(\sum_{i=1}^{n} Z_{C_i}^2(\omega_r)\right)}$$

for a resonator of length $D = \lambda/m$ with n coupling impedances $Z_{C_i}(\omega_r)$.
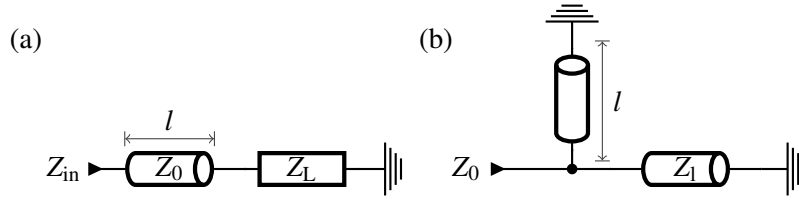

(a)   (b)

Figure 4.3: (a) A piece of transmission line of length l and characteristic impedance Z_0 connected to a load of impedance Z_L. (b) Example of an inductively coupled quarter-wavelength resonator.

In order to understand the following implementation of inductive coupling, it is instructive to inspect what an input impedance Z_{in} of transmission line with length l and characteristic impedance Z_0 connected to a load impedance Z_L, see Fig. 4.3 (a), is. The general solution for a lossless TLs for this can be found as [35]

$$Z_{in} = Z_0 \frac{Z_L + jZ_0 \tan(\beta l)}{Z_0 + jZ_L \tan(\beta l)} \quad,$$

where the propagation constant $\beta = 2\pi/\lambda$. If the stub is short-circuited, so $Z_L = 0$, this can be simplified to $Z_{in} = jZ_0 \tan(2\pi \cdot l/\lambda)$. One can easily see, that, depending on l/λ, this can be a positive and purely imaginary impedance depending on Z_0, or in other words inductive. Using this result it can easily be seen how to implement an inductive coupling: instead of a series capacitance a CPW stub is used as in Fig. 4.3 (b). This approach can be used to implement large couplings, where capacitive coupling can be infeasible as in [13].

4.3 Qubit-Resonator Coupling

The coupling from a qubit to a resonator cannot be sensibly described with the aforementioned equations. This is due to the fact, that the approximation of the dominating coupling does not apply. Comparing the classical decay rate of an LC circuit coupled to a microwave resonator to the purcell time, the qubit-resonator coupling can be found to be [13, 23]

$$g = \frac{1}{2} \frac{C_C}{\sqrt{C_q C_{TL}}} \sqrt{\omega_q \omega_{TL}} \quad, \tag{4.5}$$

where ω_{TL} is the resonators resonance frequency and C_C, C_q and C_{TL} are the coupling, effective qubit and resonator equivalent capacitances, compare to Fig. 4.4. For a more concrete example of these quantities, see Sec. 5.2.
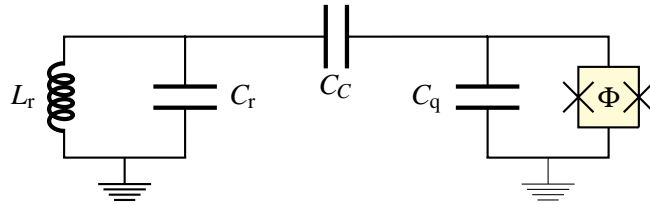

Figure 4.4: Schematic of a transmon qubit with frequency ω_q capacitively coupled to a harmonic mode with frequency ω_r.

4.4 Frequency Loading of Coupled Resonators

In the last section, it has been hinted that change in the boundary conditions also changes the resonance wavelength of the system. Furthermore, this value is required for determining the coupling strength, so in this section the loaded resonance frequency shall be determined.

Writing down the Euler-Lagrange equation [40] for a quarter-wavelength resonator coupled at one end as seen in Fig. 4.2 (a) yields

$$\frac{\partial^2 \Phi(x,t)}{\partial t^2} + \frac{1}{L_{\mathrm{l}} C_{\mathrm{C}}} \frac{\partial \phi(x,t)}{\partial x}\bigg|_{x=d} = 0 \ , \tag{4.6}$$

where $\Phi(x,t)$ is the flux as a function of space x and time t and d is the length of the CPW . It can easily be seen that the wavefunction should be of the form

$$\Phi(x,t) = \Phi_0(t) \cdot \sin(kx) \ \text{ for } \ 0 \le x \le d \ , \tag{4.7}$$

where $k = \omega/v$ is the wave-vector . Plugging this Ansatz (4.7) into the differential equation (4.6) and using $\frac{\partial^2 \Phi}{\partial t^2} = -\omega^2 \Phi$ yields

$$\tan(kd) = \tan(\omega d/v) = \frac{1}{C_{\mathrm{C}} Z_{\mathrm{l}} \omega} \ . \tag{4.8}$$

Using numeric methods, this can easily be solved to find the loaded resonance frequency, determine the required length of CPW to achieve a certain coupling at a set frequency or calculate the phase velocity from measurement data. It should be noted that the environments characteristic impedance Z_0 does not appear in this equation, meaning that the frequency of a resonator depends solely on the coupling, the physical length, characteristic impedance and phase velocity of the CPW.

In the case of the doubly coupled half-wave resonator as in Fig. 4.5 (b), there will be a voltage node in the CPW. Thus, it can be treated as two quarter-wavelength resonators and use the solution Eq. (4.8) to calculate the length, given the loaded resonance frequency (or vice-versa). Expressed in mathematical terms, the differential equation can be found to be

$$\frac{\partial^2 \Phi(x,t)}{\partial t^2} + \frac{1}{L_{\mathrm{l}} C_{\mathrm{C}_1}} \frac{\partial \phi(x,t)}{\partial x}\bigg|_{x=0} + \frac{1}{L_{\mathrm{l}} C_{\mathrm{C}_2}} \frac{\partial \phi(x,t)}{\partial x}\bigg|_{x=d} = 0 \ ,$$

with the Ansatz
$$\Phi(x,t) = \Phi_0(t) \cdot \Phi(x) = \Phi_0(t) \cdot \sin(k(x - x_{\mathrm{m}}))$$
$$\text{for } \ 0 \le x \le d \ \text{ and } \ 0 < x_{\mathrm{m}} < d \ ,$$

where d is the physical length of the TL and x_{m} the location of the voltage node, see Fig. 4.5 (a). These equations lend themselves to be solved separately, where each part is exactly like the quarter-wavelength problem.

Often, coupling is realized at the location of highest impact: voltage-anti-nodes for capacitive and current-anti-nodes for inductive coupling. However, geometrically very small capacitances
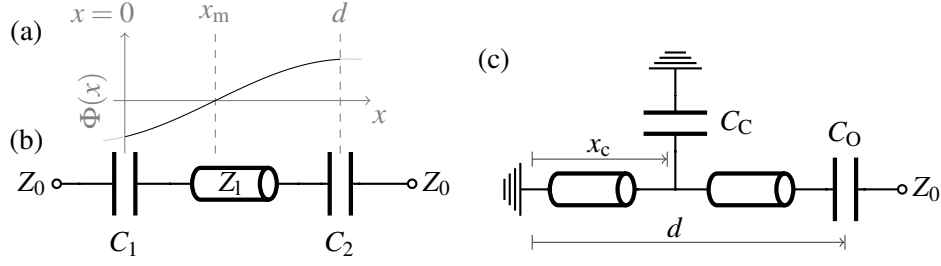
Figure 4.5: (a) Sketch of the Ansatz with arbitrary k and x_{m} used for (b) a half-wavelength TL, capacitively coupled to Z_0 environments on both ends. (c) A quarter-wavelength resonator coupled at two points. The coupling C_{C} is suppressed as a function of x_{c} (see main text).

suffer high dependency on fabrication inaccuracies and should thus be avoided. It is therefore sometimes desirable to couple at a different point, as in Fig. 4.5 (c), where a larger capacitance is required to achieve the same coupling strength. The Ansatz is [31]

$$\Phi(x,t) = \Phi_0(t) \begin{cases} B \cdot \sin(kx) & 0 \leq x \leq x_{\mathrm{c}} \\ \cos(k(x-d)-\Theta) & x_{\mathrm{c}} \leq x \leq d \end{cases},$$

where Θ is a phase and B an amplitude determined by the boundary conditions. Together with the differential equations this leads to the conditions

$$C_{\mathrm{O}}Z_1\omega = \tan(\Theta)$$
$$C_{\mathrm{C}}Z_1\omega = \tan(kx_{\mathrm{c}})^{-1} + \tan(k(x_{\mathrm{c}}-d)-\Theta) .$$

To find the according coupling strength, the previously calculated value must be corrected by the relative amplitude at the point x_{c}, which is $\langle \Phi(x=x_{\mathrm{c}}) \rangle^2 = \sin(kx_{\mathrm{c}})^2$.

5 Chip Design Procedure

The goal of this project is to investigate the feasibility of Purcell filtering for S7. In this chapter, we dissect this task into three steps; firstly, we use the quantum-mechanical description of the system to determine the desired abstract properties of the system, such as resonance frequencies of the components, coupling strengths et cetera. In the next step, we chose a concrete implementation and calculate the required geometries. Finally, a drawing, compatible with the fabrication tools, laying out these geometries needs to be created.

5.1 Readout Simulations

As discussed in Ch. 3, the differential equations provide a strong tool for simulating and optimizing the parameters of a readout system. In this chapter, we will discuss what considerations need to be taken into account in order to receive realistic and relevant results.

Equations (3.1) and (3.2) do not contain any information about physical limitations and relations between the parameters χ, g, κ_f, J and the chosen frequencies, such as eq. (2.2). Additionally, some prequisites, such as a large resonator-Qubit detuning, have to be fulfilled in order to obtain the assumed dispersive readout. Lastly, there exist limitations in some of the values that can be achieved, such as frequencies that can be processed or couplings that can be achieved. A list of these can be found in App. B. Consequentially, we have to make sure all these restrictions are fulfilled in order to ensure the used equations hold and to receive results for systems that can actually be physically build. All further steps assume, that this check has been performed and passed.

As laid out in Sec. 2.5, two-Qubit gates often require a specific frequency layout for the qubits. Since not all seven qubits are on the same feedline, we will illustrate the design procedure on the feedline with the most qubits, which is one data qubit at 6.7 GHz (DH), two ancillas at 6.0 GHz (AX and AZ) as well as two data qubits at 4.9 GHz (DL0 and DL1). Therefore, each qubit-readout-system has six undetermined parameters: ω_r, ω_d, g, J, κ_f and κ_r. With the fixed relation between J, κ_f and κ_r from (2.5) and the choice of a symmetric drive, fixing ω_d, a four-dimensional parameter space remains. Furthermore, the limited frequency range for placing the PFs and RRs of 7.0-7.8 GHz and limitations in achievable couplings needs to be considered, effectively bounding this remaining space.

For the next step, we define a value for the assignment fidelity that should be achieved for each readout and investigate the time an according readout requires. For a first approximation, we numerically solve the differential equations and determine the fidelity as a function of drive time, revealing an estimate of the readout duration. The drive is assumed as constant during the whole readout. The strength is set such, that the dispersive limit holds, expressed by the critical photon number [24]. Of course this neglects the ring-down time, any positive effect pulse-shaping or active depletion [41] can have. The time for ring-down can roughly be estimated as $2/\kappa_r$. To determine these more accurately, an iterative approach can be used. Executing these over the relevant range of the four free parameters, provides us with a useful parameter-readout-time-relation.
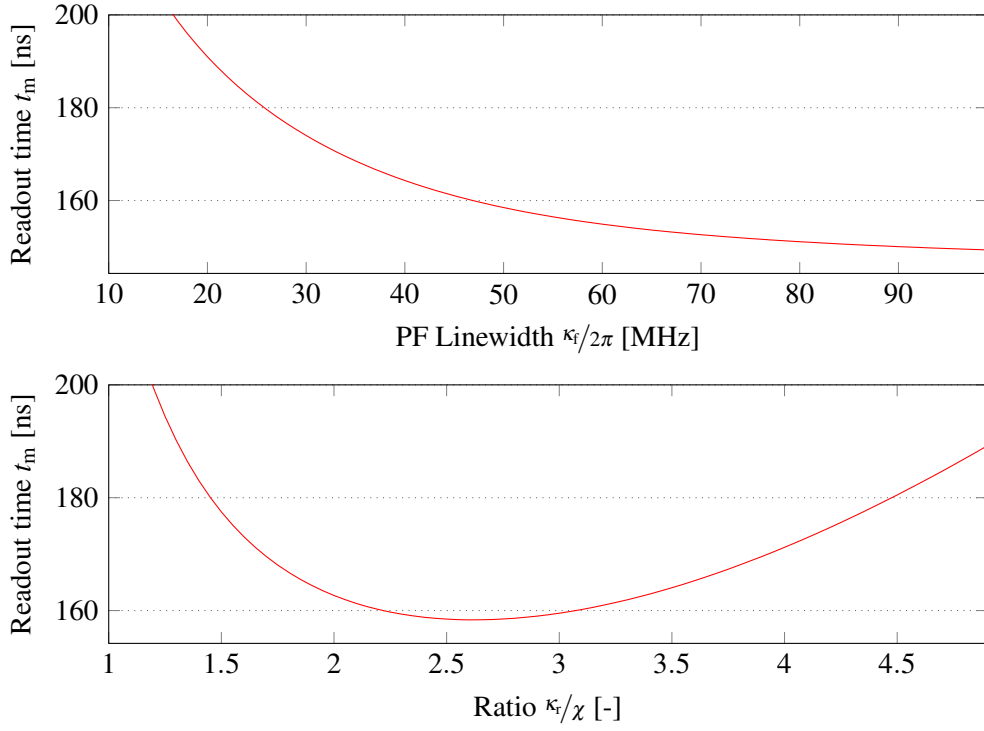
Figure 5.1: Plot of the estimated readout time as a function of κ_f with $\kappa_r/\chi = 2.5$ (top) and κ_r/χ with $\kappa_f/2\pi = 50\,\mathrm{MHz}$ (bottom), using fixed values $\omega_q/2\pi = 6\,\mathrm{Ghz}$, $\omega_r/2\pi = 7.3\,\mathrm{Ghz}$, $g/2\pi = 180\,\mathrm{MHz}$, $\delta_\alpha/2\pi = -350\,\mathrm{Mhz}$ and $\eta = 0.32$ with a fidelity threshold of 0.999.

When sweeping one parameter, while keeping the others fixed, we see a monotonic decrease in readout-time with increasing values of κ_f and g, with a sharp drop in the beginning and little gain for higher values, see Fig. 5.1 (top). The dependence on J and ω_r on the other hand show the existence of a preferable value, which is dependent on the other parameters, see Fig. 5.1 (bottom). Finally, a parameter set is found, where readout with 99.9% within 300 ns for all qubits is predicted, see Fig.5.2 (a). Note, that these simulations do not include the effect of energy relaxation or natural dephasing of the qubit, which might pose a lower upper bound to readout fidelity.
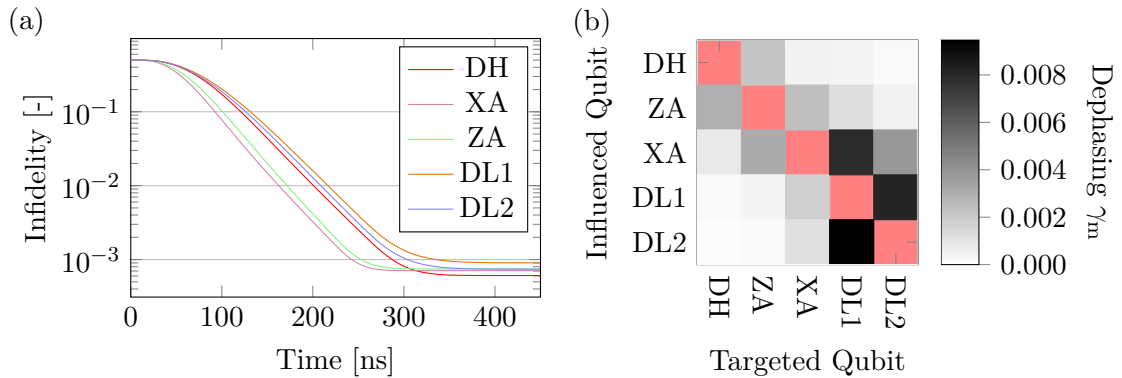

Figure 5.2: Results obtained from readout simulations using value from Tab. 5.1. (a) Infidelity of the readout result as a function of readout time. (b) Cross-dephasing matrix, showing the dephasing of an untargeted qubit if a target is read out. The elements on the diagonal (marked red) are the dephasing when measuring the qubit and are therefore left out.

The next considerations concerns crosstalk and practicalities of the readout process in S7. If a readout-pulse is Fourier-transformed, we expect a rather broad power spectrum due to its short duration. This means that, the closer two PF frequencies are to each other and bigger κ_f (*wider* PFs), the more crosstalk is anticipated. In the surface code, the ancilla qubits will be read at a much higher rate than the data qubit. This has two consequences: data qubit coherence and readout speed for ancillas should be prioritized. Furthermore, we can neglect the crosstalk between data-Qubits, since the readout will be simultaneous and can thus be classically compensated for [42].

Applying the readout-pulse of one qubit to another, non-targeted qubit, compensating for the difference in coupling to the feedline and using Eq. (3.8), we can determine a numerical estimate of the induced dephasing. The relation between all qubits can be expressed as a matrix, as visualized in Fig. 5.2 (b). Using a model of the measurement frequency, we determine the total dephasing rate, which can then be expressed as a dephasing time. This provides a very useful tool for optimization of the frequency spacing and bandwidths.

The target values derived here and in previous chapters can be found in Tab. 5.1.

Table 5.1: Target parameters for the qubits and resonator connected to the feedline with five qubits of a S7 device.

Description	Symbol	DL0	DL1	AX	AZ	DH	Unit
Bus couplings	$J_1/2\pi$			15			MHz
Anharmonicity	$\delta_\alpha/2\pi$			-290			MHz
Qubit sweetspot freq.	$\omega_q/2\pi$	4.9	4.9	6.0	6.0	6.7	GHz
RR freq.	$\omega_r/2\pi$	7.10	7.20	7.35	7.60	7.80	GHz
PF freq.	$\omega_r/2\pi$	7.10	7.20	7.35	7.60	7.80	GHz
Qubit-RR coupling	$g/2\pi$	170	170	160	170	105	MHz
RR-PF coupling	$J/2\pi$	8.3	8.2	11.4	10.7	8.8	MHz
PF-feedline coupling	$\kappa_f/2\pi$	45	45	55	55	45	MHz

5.2 Design of Qubits

In the previous chapters, the requirements for a qubit in the surface code have been reviewed. To summarize; six direct couplings to the qubit are required in total: four busses with very high couplings, one readout-line with medium coupling and one direct microwave drive with low coupling. Additionally, local control of the magnetic flux through the SQUID-loop is desired. Furthermore, a transmon consists of two islands with a capacity C_t between them and connected by the SQUID. With these constraints, the *Starmon*-Design was developed [43], an example of which can be seen in Fig. 5.3 (a). The direct connections to the individual qubits is routed through vertical connections, so-called through-silicon vias (TSVs).

Using an equivalent circuit, such as the one depicted in Fig. 5.3 (b), the effective capacitances, that will ultimately determine the couplings to the qubit, see Eq. (4.5), and the charging energy $E_C = e^2/2C_q$ [10], can be calculated [43]. These results reveal that any increase of the capacitances
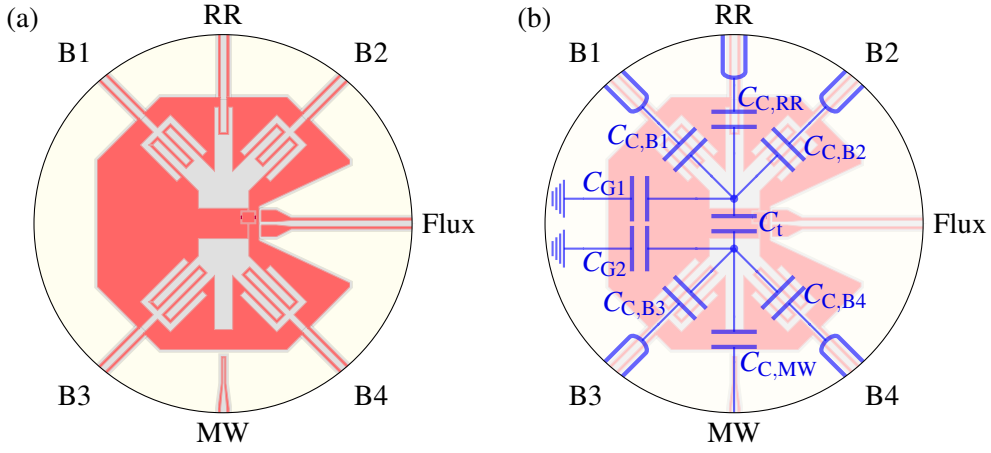
Figure 5.3: (a) Rendering showing a transmon qubit in the Starmon design. Shown are the etch-layer in red, the conductive layer in gray and the holy ground plane in light yellow (see Sec. 5.4 for details). Around it, the locations of the bus (B1-4), the RR, the fluxline and the microwave driveline (MW) connectors are marked. (b) Same rending overlaid with a simplified equivalent circuit in blue.

shown in Fig. 5.3 (b) will increase C_q and thus decrease the charging energy and all couplings towards the qubit. With the target values described in the beginning of this section and the equations of Ch. 4, one can find suitable capacitance values. The static finite-element (FE) feature of the commercial simulation software CST was utilized to extract the capacitance matrix of designed geometries, which was refined in an iterative approach to determine the exact geometry of each qubit [43].

In the surface code implementation used [1], there is a feedline on each second vertical, as in Fig. 5.4 (a). The figure also illustrates, that the island of the ancilla with the coupling to the RR is in one plaquette connected to two low- and in the other plaquette to two high-frequency qubits. The presence of the RR coupling reduces the amplitude of the bus couplings. This needs to be compensated for, leading to two different ancilla qubit designs, see Fig. 5.5 (a).
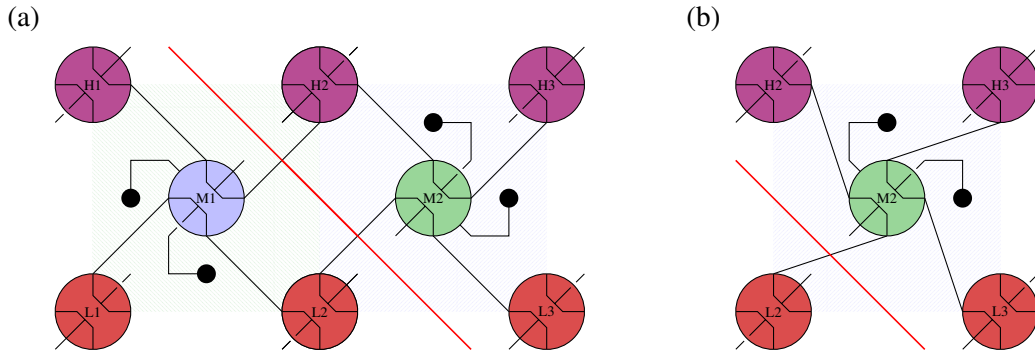

Figure 5.4: (a) Implementation of two neighboring plaquettes in the surface code. The circles schematically represent the starmons, the black dots the TSVs, the red lines the feedline and the black lines the busses. The TSVs for the data qubits have not been drawn. Both plaquettes can be either X- or Z-parity. (b) New design of the right plaquette of (a) with changed coupling (see main text).

For this work, these qubit layouts were adapted for the desired readout couplings, which as much higher than before are determined in Sec. 5.1. Due to the impact on the other couplings

when changing one capacitance, the bus capacitances needed to be adjusted accordingly. Due to the geometric limitations of the capacitors, some of the qubit-bus coupling amplitudes could not be kept at the same magnitude in this process. Equation (2.1) states however, that a decrease in bus-coupling of one qubit can potentially be compensated for by an according increase in the other qubit coupled to that bus. This does not work however, if the coupling is geometrically limited on both sides, as it is the case for the second ancilla type qubit (third from left in Fig. 5.5 (a)).
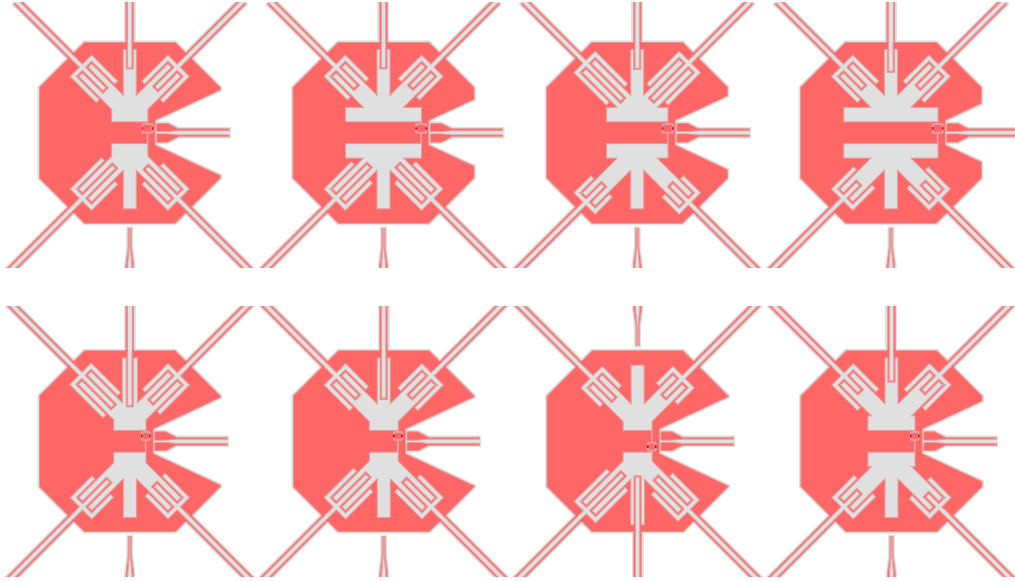

Figure 5.5: Comparison between the previously used [43] (top) and newly designed Starmons (bottom). From left to right: low frequency data, medium frequency first ancilla and second ancilla and high frequency data qubit designs.

Therefore, we investigated how the bus connection scheme can be altered to remedy this problem. In this context, three observations becomes important: firstly, larger capacitances are required to produce the couplings to the lower frequency qubits, see Eqs. (4.5). Secondly, the individual couplings need to be higher to produce equal interaction rate, see (2.1). Lastly, the mutually detrimental effect of large capacitances is stronger on the same island. With these observations, it is clear why the second ancilla type is geometrically limited: two low-frequency qubits and the RR are coupled to the same island. By rotation of the problematic qubits by $90°$ relative to the others, the same island is now coupled to both a low and a high frequency qubit, allowing for larger couplings. The currently used fabrication of the JJs does not allow for this rotation however, so the connections towards the qubit must be changed instead. With the placement of the TSVs in the current designs, this means a reflection and $180°$ rotation is required, see Fig. 5.4 (c). The final result can be seen in Fig. 5.5 (b).

5.3 Calculation of Microwave Values

In the previous section, linewidths, frequencies and couplings have been determined. In this section, we will discuss the procedure to transfer these into values required to design a chip.

The determined values are such that $J \ll \kappa_f \ll g$ there, we chose the coupling layout as in Fig. 4.5 (c), to obtain similar capacitance values for the couplings. Here, it becomes important that cQED implementations of capacitances show a rather large to-ground additionally to the desired capacitance, leading to an effective circuit depicted in Fig. 5.6. While this has little influence on the coupling strength, the coupling and to-ground capacitances must be summed in order to calculate the frequency shift (see Sec. 4.2). These to-ground capacitances are however dependent on the exact implementation of the capacitor and its target value.

Figure 5.6: Schematic of a Purcell-filtered single qubit readout setup, including the to-ground capacitances (in gray) and the qubit. For simulation with microwave software, the qubit would be excluded. P1 and P2 are $50\,\Omega$ port, used to extract the scattering matrix.

Therefore, we opted for an interdigitated capacitor design, see Fig. C.1. As illustrated in App. C, these exhibit a very linear behaviour between finger length and capacitances. After calculating the capacitance values of the couplings g and κ_f with Eqs. (4.4) and (4.5), the finger length can be determined and the to-ground capacitances estimated. The last coupling, J, has more dependences. It is therefore useful to dictate a (realistic) capacitance value for the coupling J and numerically optimize the lengths of the resonators to achieve the desired value J and frequencies. Because the couplings depend on the bare resonator frequency, an iterative approach can deliver more accurate results. Finally, the J, κ_f and frequency targeting was verified by running a microwave simulation software over the circuit of Fig. 5.6.

One last effect must be taken into account for the frequency targeting of the resonators: there is a shift induced by photon-qubit coupling at low photon number

$$\xi = \frac{g^2}{\omega_q - \omega_r} \quad , \tag{5.1}$$

called lamb shift, which needs to be compensated for accordingly.

If an input capacitor of $C_{in} = 40\,\text{fF}$ is added on the feedline, as discussed in Ch. 3, around 99% of the signal will leave through the output port [31]. Additionally, there will be standing waves

28

in the feedline. Thus, κ_f is not independent of the relative location on the feedline. This can be mitigated by either placing its capacitor at a voltage anti-node or according compensation with a larger capacitor.

5.4 Creation of a CAD

Finally, the physical parameters can be transferred into chip design, consisting of patterns for the required fabrication steps. At the date of writing this thesis, two main chip formats were in use in the DiCarlo Group. The first, so-called octobox layout, demands a $7 \times 2\,\text{mm}$ chip with eight positions for connections. These restrictions are induced by the adapter plate, a printed circuit board (PCB) with an indentation in which the chip is placed, that is used to connect to the chip. Since this amount of connections is difficult to increase using lateral connections, TSVs are used. The locations of these TSVs and the according adapter plates constitute the second chip form factor. The implementation of these requires additional fabrication steps and thus longer fabrication lead times. Therefore, for a first test device we opted for the octobox layout. With its eight connections, fluxlines and microwave drivelines for three qubits plus two ports for the feedline can be realized. Since the form-factor of $7 \times 2\,\text{mm}$ was determined to be too small for the three qubits and all the required transmission lines and resonators, the adapters were altered to allow for chips sized $7 \times 5\,\text{mm}$.

The three qubits were chosen as a subset of the five qubits in S7 that are coupled to the same feedline and connected to each other, while containing all three qubit frequencies. The chosen qubits DL1, AX and DH will, in the following be called QL, QM and QH, respectively. Besides the already discussed elements, there are some more elements in such a design that need consideration. Firstly, holes in the ground plane (to form the so-called holy grounds) are placed to trap potential vortices. The connection pads (launchers) need to be significantly larger than the TLs in order to connect to them to the PCB. To reduce reflections, a smoothed shape was chosen [44]. Thin archs spanning over TLs (airbridges) connecting groundplanes to mitigate spurious modes and charge buildup, need to be placed. Investigations of these design parameters are subject to current research [45].

All the required components are then translated into a CAD, compatible with the patterning devices. We used a python software package [45] based on gdspy [46] to accomplish this task. Some of the patterning layers, required for fabrication of the design can be seen in Fig. 5.7.
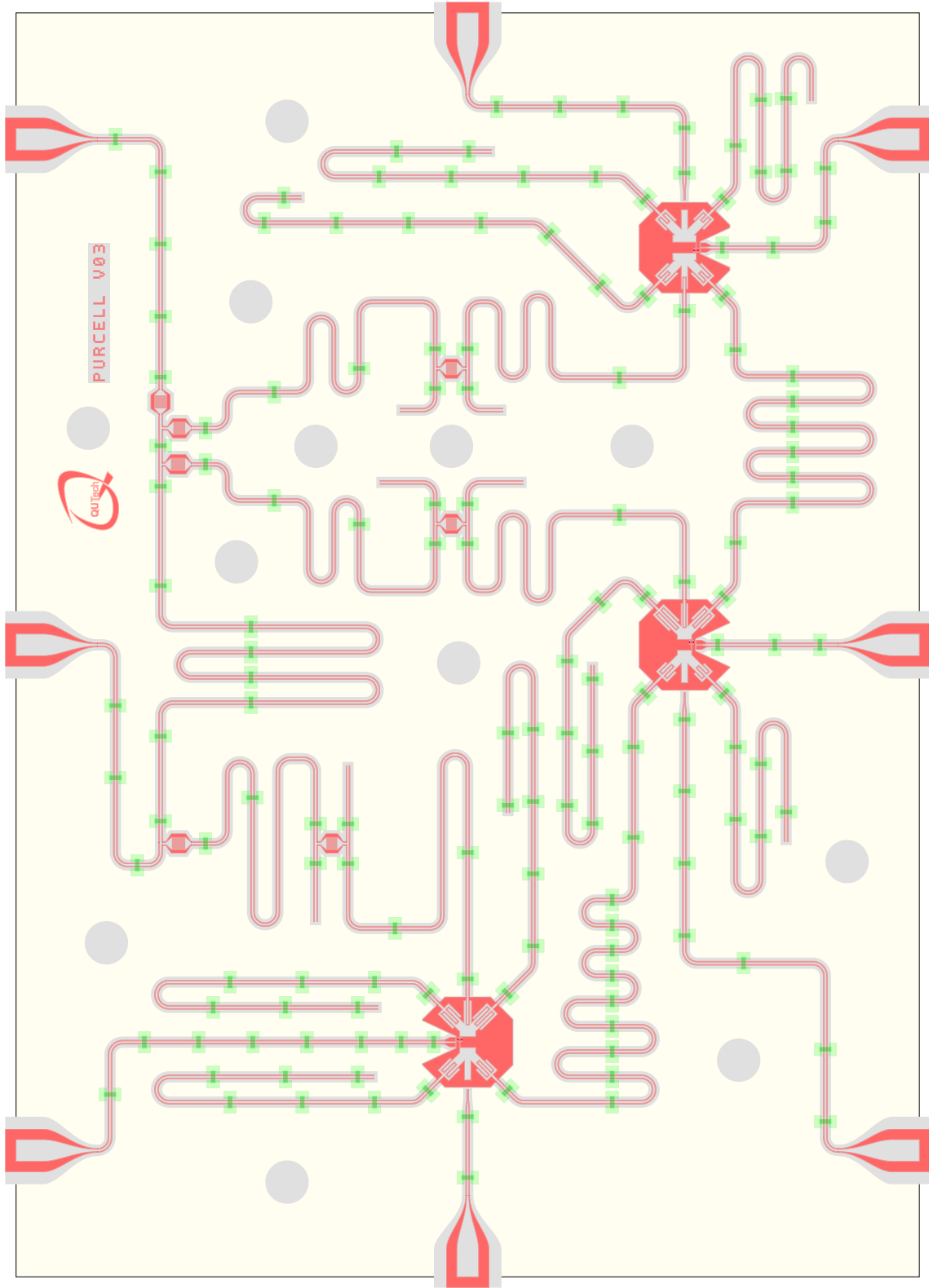
Figure 5.7: Rendering showing the etch- (red), airbridge- (green), solid- (gray) and holy-ground-layer (yellow) of the proof-of concept chip design. The etch-layer parts, that protrude at the launcher positions, prevent potential short-circuits in case the chip is not ideally cut after fabrication. The outer edge of the chip is also lined with a solid ground strip, which is not drawn here, but is visible in Fig. 5.8.
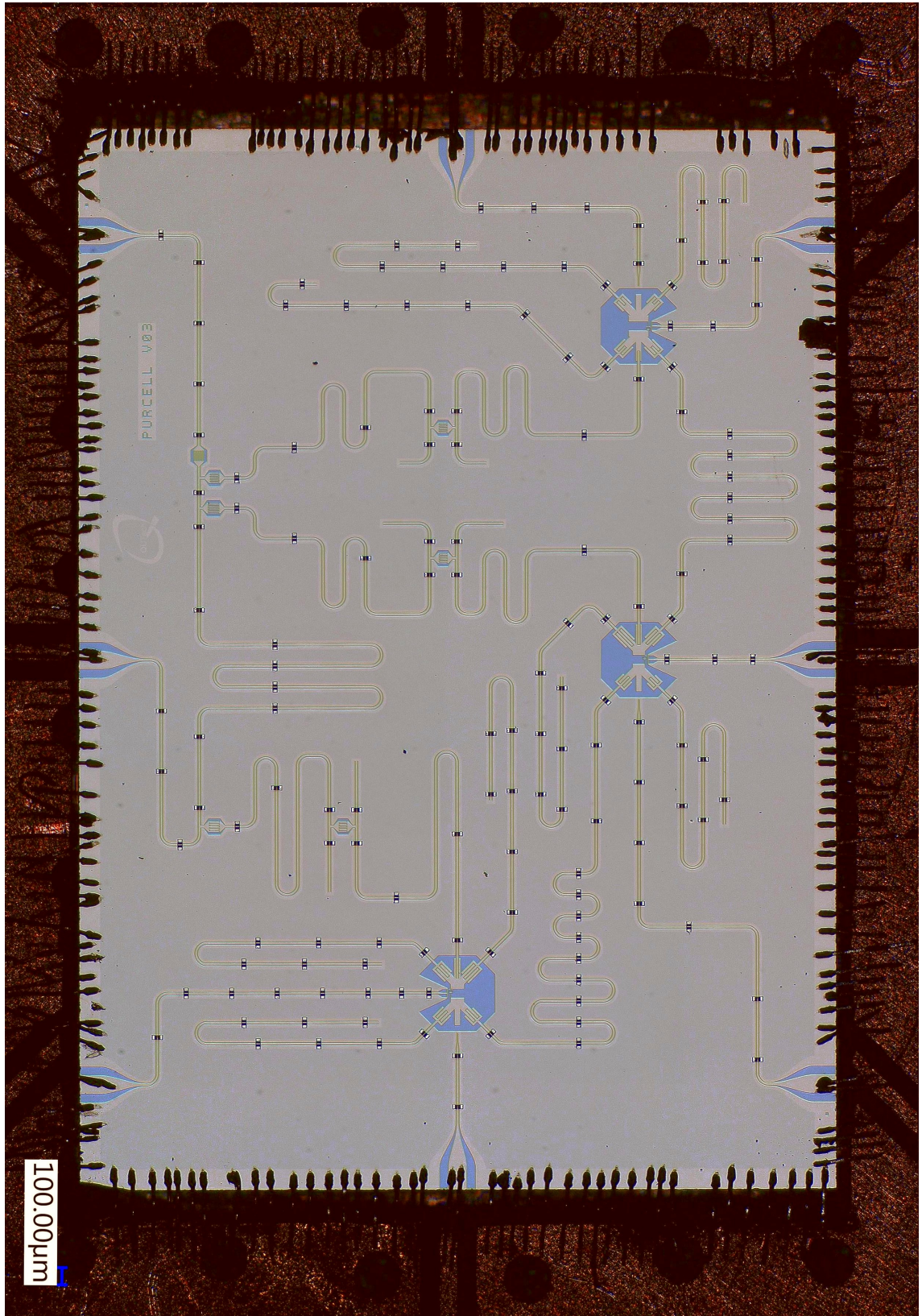
Figure 5.8: Light microscope picture of the chip in the PCB. The superconducting film appears in gray, the substrate in blue and the PCB in copper-red. Clearly visible are the wirebonds all around the chip connecting chip and PCB for grounding and signal transmission.

6 Fabrication

Here, an outline of the fabrication procedure is given. For details on the individual steps, please refer to App. E.

In the first step, a silicon waver was sputtered with a $250\,\mathrm{nm}$ thick niobium titanium nitride (NbTiN) layer. After verifying the thickness of the film, the waver was diced into smaller units, that are easier to handle. Then, the critical temperature $T_C = 14.5\,\mathrm{K}$ and room temperature resistance $\rho = 76.14\,\mu\Omega\cdot\mathrm{cm}$ were measured. Setting a fixed centre conductor of $w = 12\,\mu\mathrm{m}$ and $Z_0 = 50.0\,\Omega$, we use the formulas given in Sec. 4.1 to obtain a gap width of $s = 4.7\,\mu\mathrm{m}$ to yield $L_l = 436.7\,\mathrm{nH/m}$ and $C_l = 174.4\,\mathrm{pF/m}$ which results in $v = 114590\,\mathrm{km/s}$. When using the results for C_l found in App. A instead of the analytical expression, we obtain $s = 5.2\,\mu\mathrm{m}$, for $L_l = 448.9\,\mathrm{nH/m}$, $C_l = 178.7\,\mathrm{pF/m}$, which results in $v = 111647\,\mathrm{km/s}$. For the design, we decided to use a gap of $s = 5\,\mu\mathrm{m}$ and assume $v = 113000\,\mathrm{km/s}$ to determine the microwave geometries, listed in Tab. 6.1.

Table 6.1: Microwave geometries used for the design as fabricated. All capacitors share all parameters except the finger length, see App. C.

Description	Value			Unit
Input capacitor finger length	63.1			μm
Length input capacitor-QL coupler	6759.0			μm
Length bus QL-QM	5870.8			μm
Length bus QM-QH	5752.9			μm
	QL	QM	QH	
Capacitor J finger length	51.1	51.1	51.1	μm
Capacitor κ_f finger length	65.4	70.7	57.0	μm
PF length total	3655.3	3558.0	3375.9	μm
PF stub length	431.8	505.4	394.3	μm
RR length total	3748.7	3677.1	3523.3	μm
RR stub length	431.8	506.7	394.8	μm

With the finished design, fabrication was continued: after spinning an electron-beam (e-beam) resist on the waver, the chip layout was patterned with an electron-beam. After removing the exposed resist, reactive ion etching was used to remove the exposed film.

For the qubits sweetspot to be at the desired frequency, the JJ energy needs to be targeted. Here we use Al-AlO$_\mathrm{x}$-Al JJs. The energy is primarily determined by the geometry, i.e. overlap area and thickness of the insulating separation. Since it is very sensitive to the exact fabrication procedure, arrays of test-junctions were deposited onto another waver and the JJ energy was estimated by measuring their room-temperature resistances. The JJs were then deposited using double-layer resist of different sensitivities and two-angle shadow-evaporation.

For the airbridges, several layers of resist with different sensitivities were spun and exposed in the e-beam, resulting in a block of resist with two areas of exposed base-layer. The block was reflowed to achieve the curvature of the bridges. Aluminium was then evaporated on the sample to

form the bridges.

After using a dicer to extract the chips from the tile, another room-temperature resistance measurement of the JJs was conducted and the sample closest to target was selected. These measurements indicated, that even for this chip, the Qubit frequencies are expected to be significantly above target. Next, the chip was placed in an accordingly sized indentation of a PCB. Using a wire-bonding device, the launchers were connected to PCB traces connecting them to SMP connectors and connections around the chip for grounding were placed. Figure 5.8 shows a light microscope picture of the result.

7 Measurements

In order to conduct measurements on the device, the chip in the recess of the PCB is placed inside a copper housing to shield any radiation while ensuring good thermal contact and protection from environment photons. This housing is in turn bolted onto a metal rod and connected with coaxial cables, see Fig. 7.1 (d). After adding several radiation shields, this so-called satellite is installed inside a Leiden Cryogenics dilution refrigerator. The fridge is then cooled to 10 mK. All fluxlines are low-pass filtered and connected with DC sources. The microwave drivelines and feedline input are connected to an arbitrary waveform generation chain and the feedline output to an analogue to digital translation chain, after passing through a high electron mobility transistor (HEMT) amplifier at 3 K.
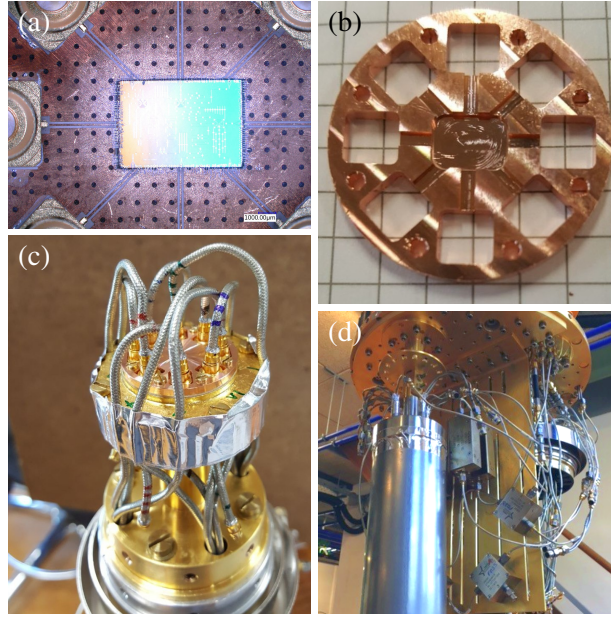
Figure 7.1: Fotographs showing (a) a zoom-out of the PCB with chip and parts of the SMP connectors. (b) the upper half of the copper housing. The recess in the middle matches the chip, the square holes the SMP connectors. (c) the device installed on a coldfinger inside a satellite. (d) the satellite with shielding layers installed on the lowest stage of the dilution refrigerator.

As already indicated by the room-temperature measurements of the SQUID resistance, the qubits sweetspot frequencies are much higher than intended. This can be attributed to a mechanical malfunction in the shadow evaporation machine, which hindered precise deposition of the JJs. Furthermore, for the measurements presented below, the fluxline of QL is not correctly connected and QL is thus not (directly) flux-tuneable. The limited tunability through crosstalk from other qubits is not sufficient to bring it to the target frequency. Consequentially, most of the following measurement are limited to QM and QH.

Table 7.1: Measured and directly fitted (upper part) and deduced (lower part) values. Values marked with a dash could not be determined.

Description	Symbol	QL		QM		QH		Unit	Note
		meas.	target	meas.	target	meas.	target		
Readout resonator frequency	$\omega_r/2\pi$	-	7.200	7.134	7.350	7.558	7.800	GHz	With qubit at target frequency
		7.070						GHz	With qubit at sweetspot frequency
Purcell filter frequency	$\omega_f/2\pi$	-	7.200	7.149	7.350	7.572	7.800	GHz	With qubit at target frequency
		6.949						GHz	With qubit at sweetspot frequency
Dispersive shift	$\chi/2\pi$	-	-2.8	-4.9	-6.7	-4.5	-4.2	MHz	
Lamb shift	$\xi/2\pi$	[115.1]		21		16.4		MHz	
Purcell filter to readout resonator coupling	$J/2\pi$	[32.8]	7.67	27	11.36	35	8.81	MHz	
Purcell filter to feedline coupling	$\kappa_f/2\pi$	23.1	45	25.5	55	17	45	MHz	
Qubit sweetspot frequency	$\omega_{q,max}/2\pi$	6.63	4.90	6.97	6.00	7.00	6.70	GHz	
Energy relaxation time	T_1	1.0		1.6		6.0		μs	With qubit at target frequency
		-		20		15		μs	With qubit at sweetspot frequency
Dephasing time	T_2^{echo}	1.6		1.6		6.0		μs	With qubit at target frequency
		-		3.0		8.0		μs	With qubit at sweetspot frequency
Anharmonicity	$\delta_\alpha/2\pi$	-290		-276	-290	-272	-290	MHz	With qubit at target frequency
Quantum efficiency	η	-		6.6		7.2		%	With qubit at target frequency
Residual excitation	p_{res}	-		2.2		3.8		%	With qubit at target frequency, using no post-selection
				0.8		0.1		%	With qubit at target frequency, using post-selection
QM-QH coupling	J_1	-		16.5	15	16.5	15	MHz	With QM at 6 GHz, moving frequency of QH
Charging energy	E_C/h	-		257		253		MHz	Calculated from δ_α
Qubit-resonator coupling	$g/2\pi$	170	160	169	160	128	105	MHz	Calculated from χ
		170	160	155	160	109	105	MHz	Calculated from ξ
Critical photon number	n_{crit}	-		11.4		11.5			Calculated using g from χ
				13.6		13.2			Calculated using g from ξ
Av. photon number	$\langle n\rangle$	-		10.1		9.3			During readout. Estimated from dephasing, χ and κ_{eff} [47]

7.1 Microwave Characterization

Firstly, the basic characteristics of the readout resonators were extracted: measuring the complex transmission of the feedline and fitting the data with and equation similar to Eq. (3.10), can be used to determine the resonance frequencies ω_r and ω_f as well as couplings κ_f and J. Due to the influence of the further signal path, additional terms for phase-wrapping, frequency-dependent amplification and attenuation strength as well as impedance mismatches were introduced for the fit function, resulting in Eq. (F.1). Four such measurements for QM and QH in both computational
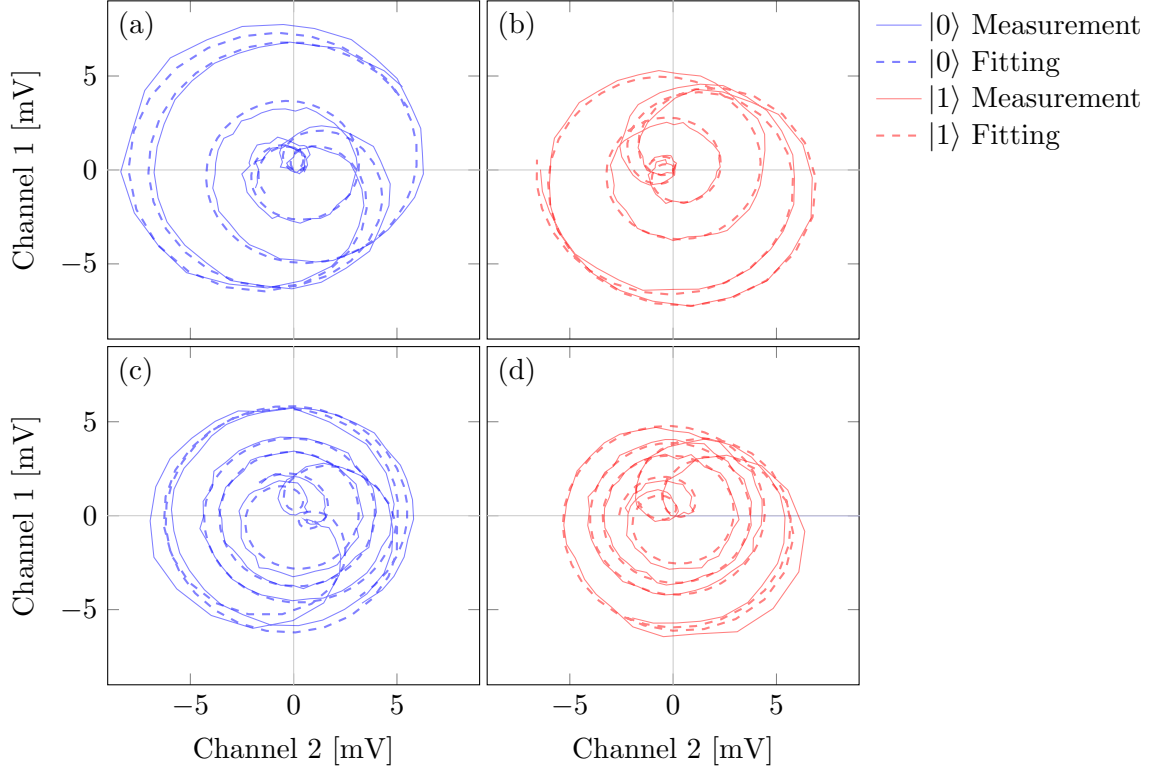
Figure 7.2: Absolute values of the measured transmission spectrum for (a,b) QM and (c,d) QH with the qubits at their respective target frequency. Here, (a) and (c) were taken with the qubits in the ground and (b) and (d) in the excited state. Overlaid is the fit, that was used to extract the parameters (see main text).

states are shown and fitted in Figs. 7.2 and 7.3. Although all four fits were conducted independently from each other, all parameters, except for the frequencies, were almost identical for the respective two states. Furthermore, dispersive shift can then be extracted by comparing the RR frequencies of the ground and excited state. The result of these measurements can be found in the first lines of Table 7.1. Using Eq. 2.2 and the later measured qubit frequency and anharmonicity, the RR-qubit coupling g is estimated.

The lamb shift does not occur in the high phonon regime. Therefore, extracting the resonator frequencies at low and high drive powers can be utilized to quantify the shift. This value can be used with Eq. (5.1) to cross-verify g, finding a very good correlation, see Tab. 7.1.
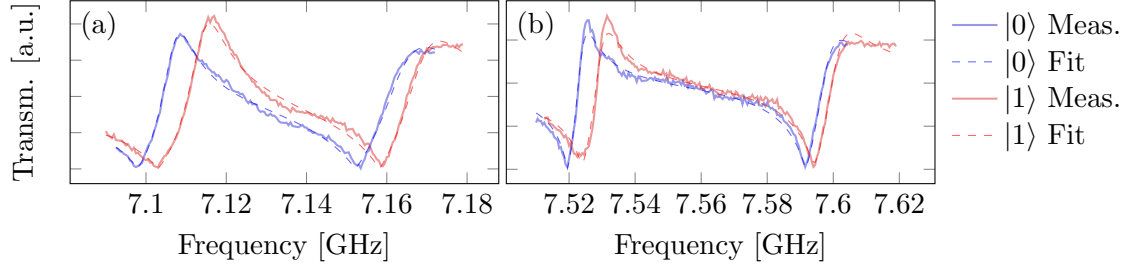
Figure 7.3: Absolute values of the measured transmission spectra for (a) QM and (b) QH in both computational states. The data and fits are the same as in Fig. 7.2.

7.2 Evaluation of the Microwave Calculations

As commented in Sec. 7.1, the fabricated device showed quite a few discrepancies in resonator attributes compared to their respective targets. Here, we analyse this and try to conciliate it with the theoretical predictions. The below-target frequencies can somewhat consistently be explained by a C_l and L_l different from the estimate given in Sec. 6. To put it more quantitatively, one can express the sum of the absolute difference between the analytically calculated values as a cost function and optimize for the lowest value. However, due to the very limited amount of datapoints, there is a region of these parameters that almost equally well fits the measurements, see Fig. 7.4.
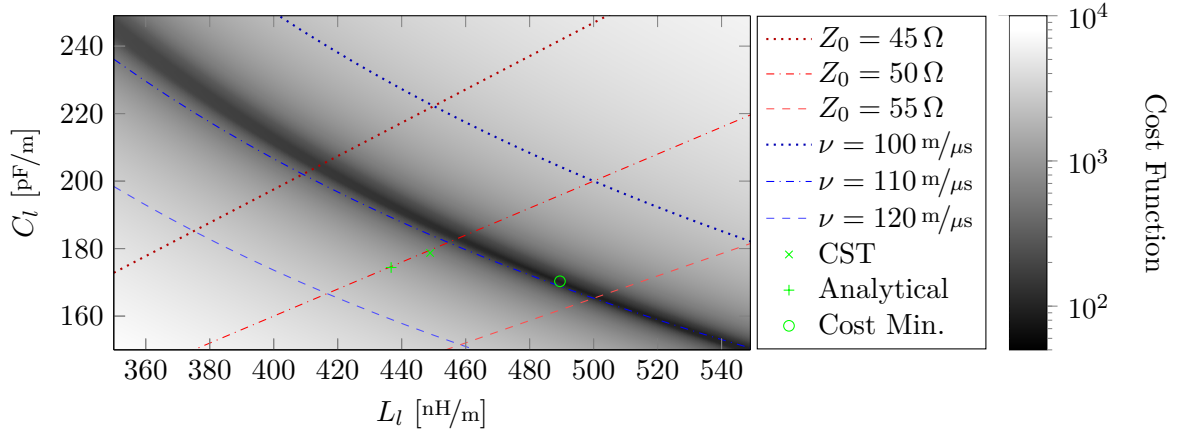
Figure 7.4: A cost function, defined as the sum of the absolute difference between the analytically calculated resonator frequencies, plotted against the inductance and capacitance per unit length. Marked are lines of characteristic impedance and constant phase velocity (dashed and dotted lines) as well as the previously calculated expectation for the used film (crosses), see Ch. 6 and the numerically found minimum (circle). Here, QL was ignored in the cost function, since it is potentially not coupling to a voltage-anti-node on the feedline, making predictions much less reliable. Including QL does not qualitatively change the landscape.

Explanation of the found couplings was not successful with this model. All capacitors used for the PF-RR and PF-feedline coupling are the same geometry with only the finger length l_{fi} varied. Simulations, shown in App. C, suggest, that the capacitance scales linear in l_{fi} for the used regimes. Therefore, we can say with a high degree of confidence, that the capacitance of the PF-RR couplings is much higher than those of the PF to feedline (compare to Tab. 6.1). Furthermore, the former coupling is implemented by placing the capacitor close to the voltage node, strongly decreasing the effective coupling. For the hole regime shown in Fig. 7.4, this results in much higher κ's than

J's for all qubits, according to the calculations done in Ch. 4. Why the measurements indicate otherwise remains unknown at this point. Patterning inaccuracies in fabrication seem unlikely, because the used e-beam lithographies resolution is several orders of magnitude below the used feature sizes for the capacitors.

7.3 Time Domain transmission

In order to verify the photon field trajectory approach outlined in Ch. 3 and Sec. 5.1, time domain traces of readout processes with the qubit separately prepared in either the $|0\rangle$ or $|1\rangle$ state were recorded. For this, the output from the feedline was down-converted with an intermediate frequency (IF) between the two according drive frequencies. The resulting signal was digitalized with the UHFLI Lock-in Amplifier of Zurich Instruments. The remaining frequency offset was digitally removed, such that all presented data here is in the rotating frame of the drive frequency.
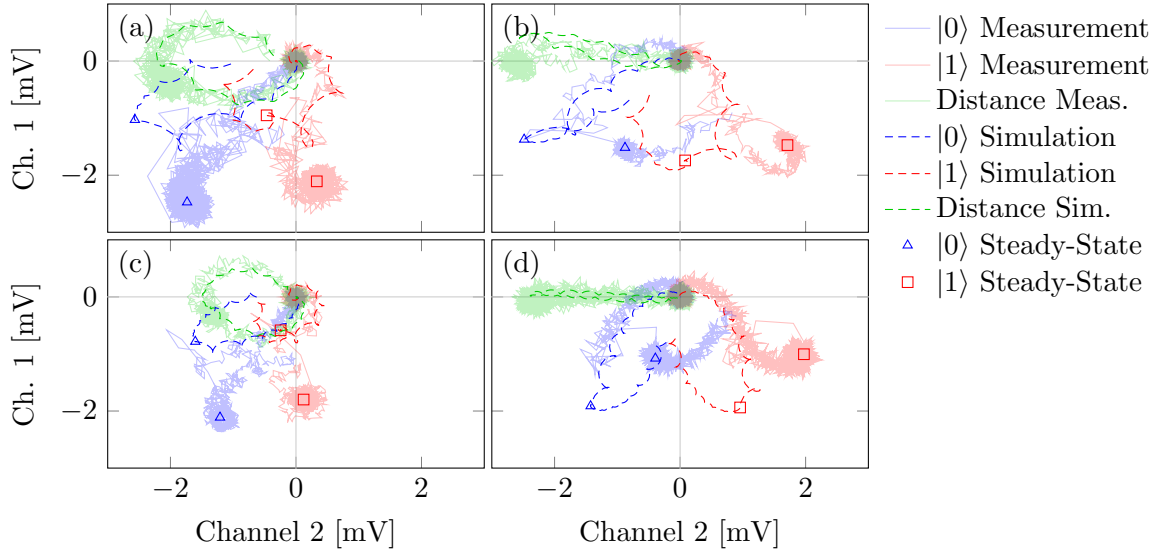
Figure 7.5: Four sets of measured state-dependent, highly averaged (10^{15}) readout trajectories and the distance between the two. Overlaid are simulation results using the fitted parameters and the used drive frequency with arbitrary amplitude and rotation. For both datasets the steady-state is marked. In (a) QM was targeted with a 300 ns long square-wave drive of frequency $\omega_d/2\pi = 7.115$ GHz. In (b) the frequency was changed to $\omega_d/2\pi = 7.111$ GHz. For (c) QH was read-out at $\omega_d/2\pi = 7.531$ GHz in 450 ns and in (d) at $\omega_d/2\pi = 7.526$ GHz also in 450 ns.

Inserting the values obtained in Sec. 7.1 into the approach of simulating the readout and comparing the resulting averaged trajectories with the measured analogon, allows us to cross-verify the fits and the simulations we used to determine the parameters in the first place. At first glance, the comparison for different readout-times and frequencies does not seem to show a strong resemblance. However, if the trajectories are split into the ramp-up and -down parts, as in Fig. 7.6, the resemblance becomes very clear. It appears as if both trajectories start with a fixed offset and after reaching steady state the same offset in opposite direction observed. Most notably, these discontinuities appear at the same time on both trajectories and thus do not influence the distance between them, which is most clearly seen in Fig. 7.7, which shows the absolute of the weight function (3.6).
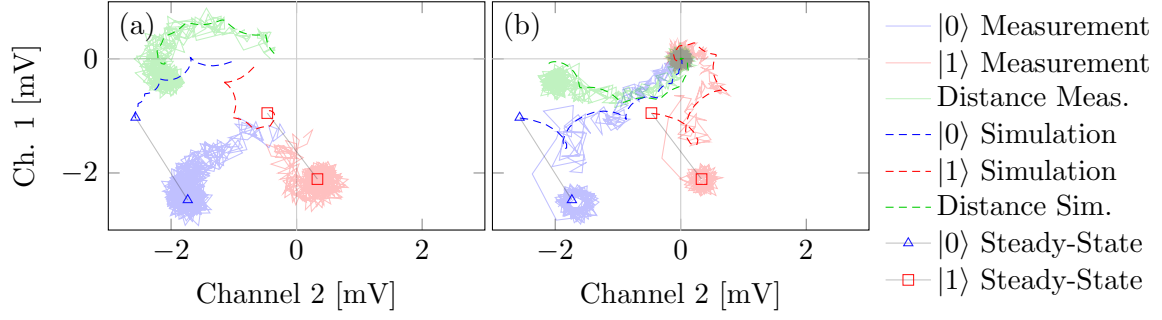
Figure 7.6: Data from Fig. 7.5 (a), split into the the (a) ramp-up and (b) ramp-down process. The steady-state points are connected by a line to highlight the offset characteristic of the discrepancy.
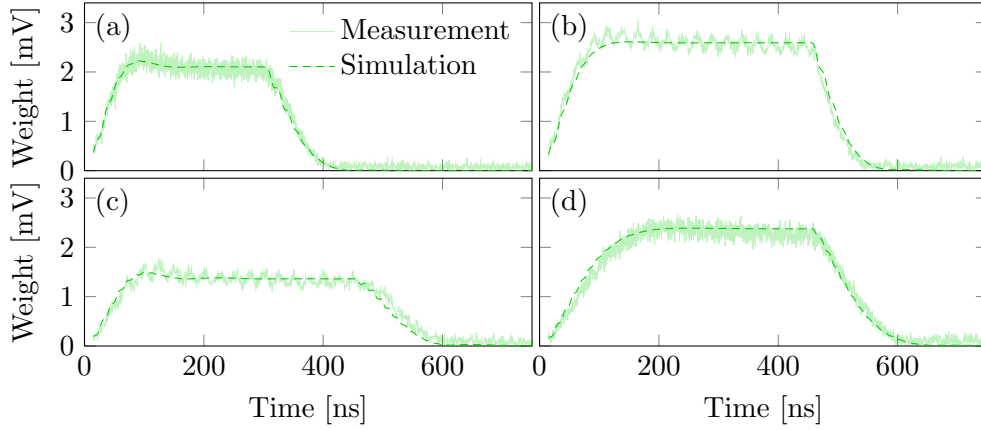

Figure 7.7: The absolute distance between the state-dependent trajectories of the four sets depicted in Fig. 7.5.

It should be noted, that the amplitude and global phase of the simulated signal was scaled for the distances to match at steady-state. This is due to the fact, that we did not quantify the influence of the signal path as influenced by input capacity, impedance mismatch at the wirebonds and most importantly the amplification chain. We attribute the measured discrete offsets to either impedance mismatches in the signal path or some inaccuracy in the data acquisition process.

These results show both the great predictive power of the simulation approach chosen as well as the working extraction of parameters from transmission measurements in Sec. 7.1. Since the distance is what determines the measurable signal, this match also verifies the applicability of the approach to optimize the parameters for fast readout. The origin of the offsets in the trajectories is subject to further investigation.

7.4 Qubit Characterisation

We next measure the qubit properties: transition frequency and coherence and dephasing times as a function of the applied flux, anharmonicity as well as the coupling to other qubits, required for two-qubit gates.

The transition frequency can be found with qubit spectroscopy. This procedures requires probing of the feedline transmission at ground state, see Fig. 7.3, while applying a continuous tone through the microwave driveline at frequency ω_{spec}. Under the condition of $\omega_{\text{spec}} \simeq \omega_q$, the qubit is taken out of the ground state, and due to the dispersive interaction between qubit and RR, the transmission of the feedline at the resonator frequency will thus be changed by the drive tone. This can be utilized to find the qubits transition frequency and associate features in the transmission with certain qubits. By plotting the transmission at the ground state frequency as a function of both ω_{spec} and the flux line current, as in Fig. 7.8, the dependency between the two can be extracted. The maximum of this curve is found at the current and frequency at which the qubit is at its sweetspot and the period relates the current with the magnetic field in the SQUID.
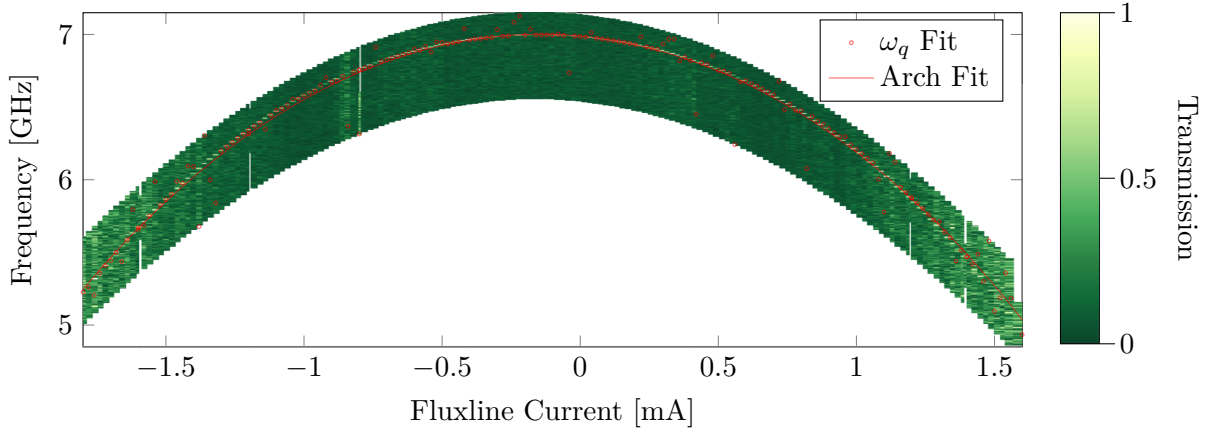
Figure 7.8: Spectroscopy scans of QH for different on-chip fluxline currents. For each scan a the frequency of the used resonator minimum (see main text) was determined first, then the qubit Frequency ω_q was fitted (overlaid in red circles). The fit with Eq. (F.2) of these is overlaid with a red line.

With the knowledge of the qubits resonance frequency (given a certain flux current), single qubit gates can be effectuated by applying resonant pulses on the microwave driveline. The duration and amplitude determines the polar angle Θ of the rotation in the Bloch sphere, while the phase determines the azimuthal angle φ. The required ratio of drive strength and duration can be found by measuring the excited state population while varying these parameters. We used a fixed length pulse convoluted with a Gaussian shape of width 5 ns and varied the amplitude to optimize for $\pi/2$ and π rotations.

The energy-relaxation time T_1 can be found by fitting the percentage of measurement outcomes declaring the qubit in the excited state as a function of wait time after preparing the qubit in the excited state with an exponential decay. The dephasing time can be measured with a Ramsey-type experiment. Here, the qubit is prepared in the superposition state. After a wait time τ, a quarter rotation around the x-axis projects the phase of the state on the z-axis, which allows measurement in that basis to, in effect, measure the phase. The result is an oscillation with the frequency difference between qubit and drive $\Delta_{qd} = \omega_q - \omega_d$ and an amplitude decay due to dephasing. Fitting the exponential decay allows to extract the dephasing time. Here however, we use the Echo-type measurement, which removes inhomogeneous/deterministic dephasing (that might be counter-acted by using exactly this sequence or according gates) by including and additional half-rotation exactly

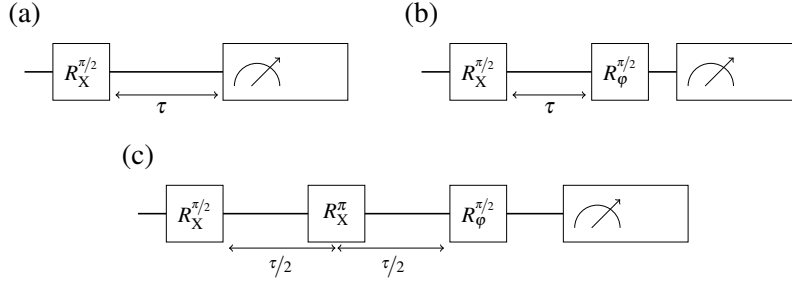in the middle of the wait time, see Fig. 7.9.

Figure 7.9: Circuit representation of the possible coherence and dephasing measurements. Here R_φ^Θ denotes a rotation with the polar angle Θ and azimuthal angle φ. (a) Energy-relaxation time measurement. (b) Ramsey-type measurement. (c) Echo-type measurement.

Figure 7.10 shows T_1 and T_2^{echo} as a function of qubit frequency for QM and QH. The fact, that resonators are below their target in frequency means that the Purcell rate at the sweetspot is very high, which leads to low coherence times there. However, when fluxing the qubits to the target frequency, the coherence time increases drastically. Utilizing Eq. (2.4) to calculate the Purcell rate and overlaying it on the measured data, shows that the coherence time of the qubit is clearly not Purcell-limited any more at the target frequency. The theoretic predictions here are $T_1^{\text{Purcell}} = 782\,\mu\text{s}$ for QM and $168\,\mu\text{s}$ for QH. At the same time T_2 is expected to be highest at the sweetspot, due to first-order flux noise insensitivity there. For QM this is however not the case, since $T_2 \leq 2T_1$ and T_1 is low due to the Purcell effect there. For QH we see such a peak just below the sweetspot, since T_1 is not Purcell-limited any more at that point.
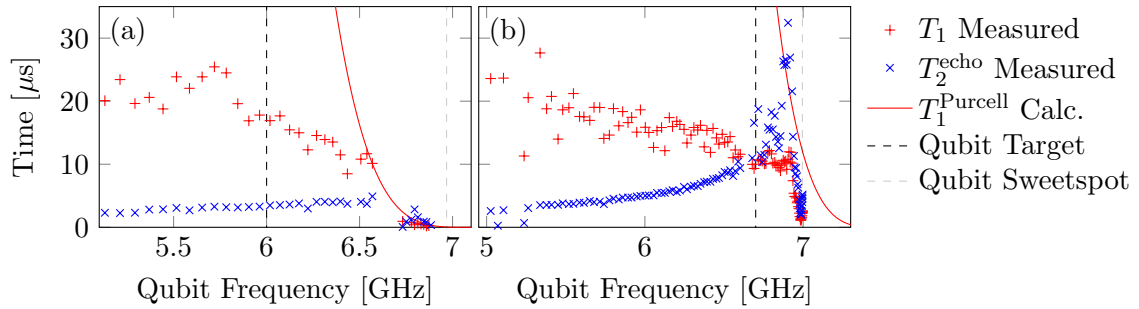
Figure 7.10: Coherence and dephasing times T_1 and T_2^{echo} as a function of qubit frequency for (a) QM and (b) QH. Overlaid is the target frequency and the calculated Purcell limit. For (a) there is a gap in data due to a crossing with QL and thus unreliable data.

The anharmonicity of a qubit can be quantified by measuring the frequency of the $|1\rangle \leftrightarrow |2\rangle$ transition and subtracting the one for the computational states. Adding a second tone to the spectroscopy will create a clear signature for either of the tones to be resonant with either transition or virtual two-photon transitions $|0\rangle \leftrightarrow |2\rangle$. Linear fitting of the resulting data accurately yields both frequencies and thus the anharmonicity δ_α. At the target frequency, we measured $\delta_\alpha = 276\,\text{MHz}$ and $272\,\text{MHz}$, which is very close to the designed-for $290\,\text{MHz}$. Using numerical optimization of the full transmon Hamiltonian, E_C can be estimated to $E_C = 257\,\text{MHz}$ and $253\,\text{MHz}$ for QM and QH, respectively.
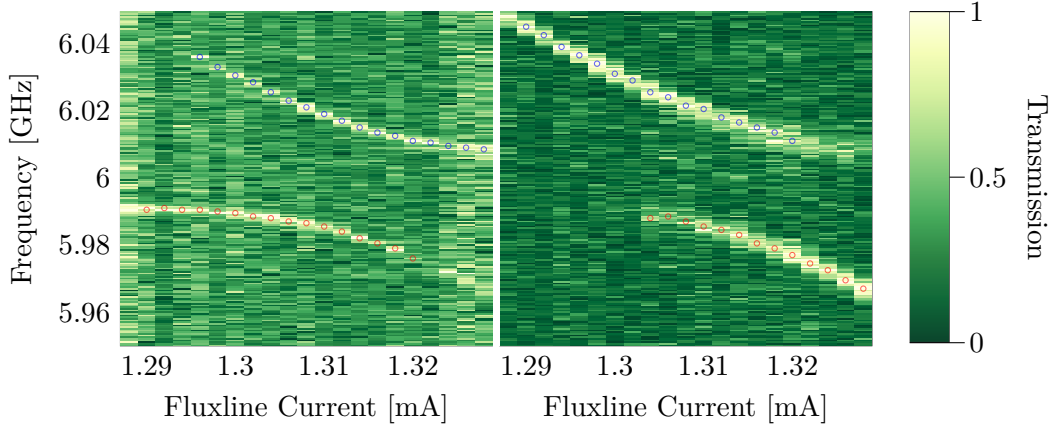
Figure 7.11: Spectroscopy traces versus QH fluxline current as measured from (a) QM and (b) QH. Circles mark the fitted frequencies of the Qubits. An avoided crossing due to bus-coupling is clearly recognizable.

Evaluation of the qubit-qubit coupling can be done through assessment of the avoided crossing, which can clearly be seen in spectroscopy on either of the qubits. Both spectroscopies on QM and QH, shown in Fig. 7.11, consistently show an avoided crossing with a separation of 33 MHz, which means $J_1/2\pi = 16.5$ MHz or a lower bound of 43 ns for an CZ gate, which is well on target.

7.5 Single-Shot Readout Characterisation

A major goal of this work is to improve the qubit state readout without limiting the lifetime of the qubit via Purcell decay. As we have shown in the previous section, the qubits are far removed from being Purcell-limited at their target frequencies. Here, we investigate the quality of the achieved single-shot readout.

As seen in Figs. 7.5, a difference in the complex photon-field trajectories is expected, depending on the qubit state. If the time-domain integrated components of these trajectories are repeatedly measured, the obtained values plotted in a two-dimensional plane show two grouping, that can be associated with the $|0\rangle$ and $|1\rangle$ state of the qubit. The data is then rotated by the angle of the axis connecting the centre-points of the groupings. Projection of the counts on this new effective integration voltage V_{eff} axis and binning the shots resulting in a double-Gaussian histogram. This allows to find a decision boundary to obtain a discrete value for the readout result. Preparing the qubit in a computational state before measurement, yields two such histograms. Fitting these, allows to characterize the readout, as exemplified in Fig. 7.12 and described in detail in App. F.

To purify the state before conducting the readout, heralded measurement can be used [48]. This is implemented by measuring the state once directly before preparing the state and discarding experiments where the outcome of the first measurement does not indicate the ground state. Such measurement results, as seen in Fig. 7.13, allow a more pure characterisation of the readout fidelity by reducing the influence of the thermal population.

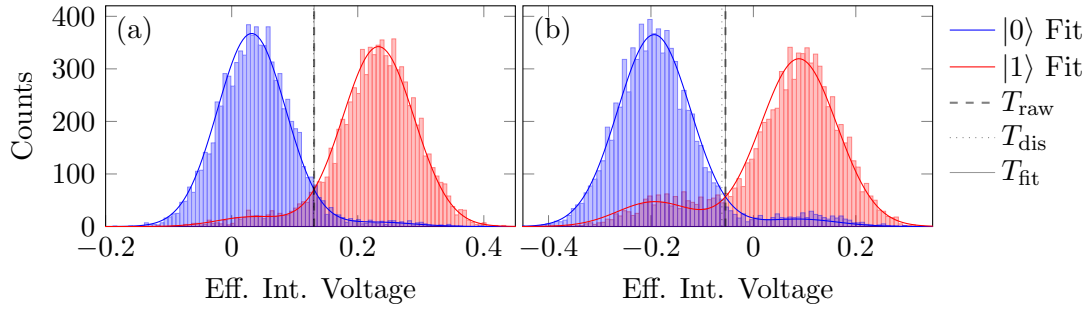The addition of the input capacitor is intended to raise the quantum efficiency by lending

Figure 7.12: Histogram of integrated voltages projected on a single axis of single-shot readouts for (a) QM and (b) QH. The blue (red) bars show outcomes where the state was prepared in the $|0\rangle$ ($|1\rangle$) state. Fitting of this data (see main text) allows extraction of SNR and fidelities.
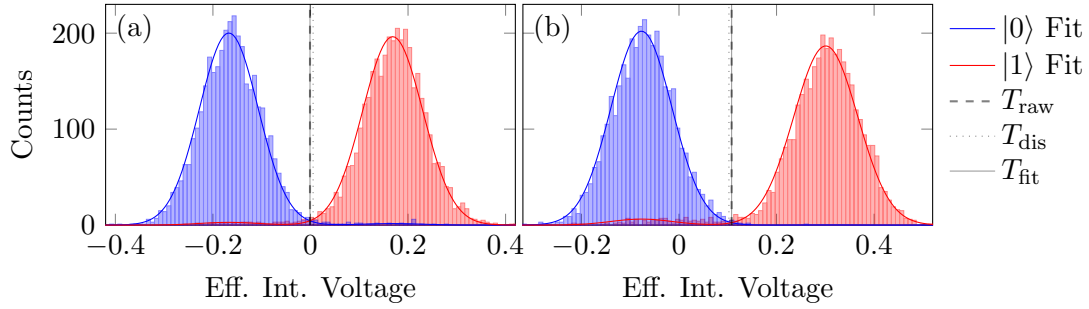

Figure 7.13: Same type of measurements as in Fig. 7.12, but with post-selection (see main text).

directionality to the signal path. Intuitively, this efficiency should be obtainable from the relation between the information that can be extracted from a readout process SNR versus the dephasing γ_m of the qubit as the measurement projects it. Indeed, this relation is given as [32]

$$\gamma_m = \frac{\text{SNR}^2}{4\eta} \ ,$$

under the condition of zero-field in the resonators before and after the readout and optimally retrieving the information from both readout quadratures using optimal integration functions.

Due to the assumed linearity of the resonators (see Ch. 3), the amplitude of the photon fields is expected to be linear in the amplitude of the drive. With Eqs. (3.7) and (3.9) we can thus see, that the SNR is linear in the drive amplitude ε, while $\gamma_m \propto \varepsilon^2$. The coherence element of the density matrix $|\rho_{01}|$ can be measured by conducting (partial) readout in the wait time of an Echo-type measurement, compare to Fig. 7.15 (b). Sweeping the azimuthal angle φ of the final gate by means of changing the phase accordingly, allows to distinguish the deterministic phase shifts (e.g. due to the ac stark shift) from non-deterministic dephasing. Inserting the γ_m–ε relation into Eq. (3.8), yields, that $|\rho_{01}|$ should show a Gaussian behaviour in ε:

$$|\rho_{01}| = \rho_{01}^\tau \cdot e^{-\frac{1}{2}\left(\frac{\varepsilon_{\text{rel}}}{\sigma}\right)^2} \tag{7.1}$$

with $\varepsilon = \varepsilon_{\text{rel}} \cdot \varepsilon_{\text{max}}$ and ρ_{01}^τ the coherence element after the measurement time τ. Using this as a fit and fitting the extracted SNR linearly, as shown in Fig. 7.14, one can thus find the constant η that relates these two values [32].
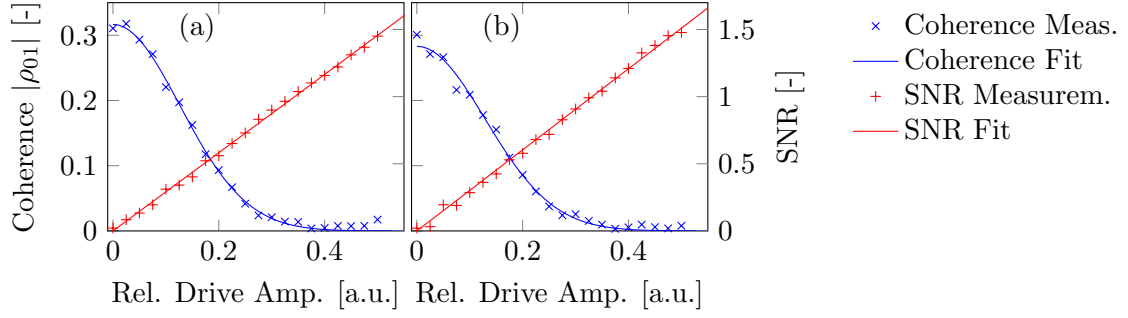
Figure 7.14: Coherence element measured with an Echo-type sequence and readout SNR as a function of drive amplitude for (a) QM and (b) QH, with according fits to extract the quantum efficiency η (see main text). The coherence shows a smaller than unity value at zero RO amplitude, due to the natural dephasing during the fixed circuit length.

Despite the deviations of frequencies and couplings from the targets, state of the art readout fidelities [13, 31, 48] of 98.7% for QM and 98.3% for QH within 450 ns are achieved. The infidelity is dominated by qubit relaxation during the readout. With the addition of parameteric amplification (e.g. with a traveling wave parametric amplifier (TWPA) [49]), we expect >99% fidelity readout within 150 ns, since a roughly five times higher quantum efficiency can be expected [31]. Using a TWPA directly on the output of the feedline would also protect the qubit from the thermal noise of the HEMT, reducing the thermal population.

7.6 Measurement-Induced Cross-Dephasing

In this Section we investigate the effect readout on one qubit has on a second qubit. As in the quantum efficiency measurements, we use and echo-type experiment to extract the dephasing effect on a non-targeted qubit. Notably, the intermediate (partial) measurement is performed on another qubit than the echo-experiment, see Fig. 7.15 (b). Using parameters for readout, such that they achieve similar SNRs, ensures that the cross-elements are comparable in the context of the Surface code.

The coherence time of QL was too low at its sweetspot, so that the experiment could only be conducted with QM and QH. Furthermore, we chose the Echo-type sequence to increase the sensitivity of the signal. The measurement, shown in Fig. 7.16, shows no clear Gaussian decay within the used amplitude window. As such, only an upper bound can be given on the cross-dephasing effect of the readout. Assuming a lower bound of 10 for σ (compare to Eq. (7.1)) of the cross-elements, equates to a reduction of the coherence element of 0.5% per measurement. Repetition of this readout every microsecond thus results in an induced decoherence time of $T_2^{cr} = 200\,\mu$s. This upper bound would be far above what we targeted, especially when taking into account, that due to the large RR spacing, the investigated contribution should be very small compared to those with smaller spacings. Therefore we have to conclude, that we have no conclusive data at this point, that would allow any serious comparison to the predicted crosstalk.
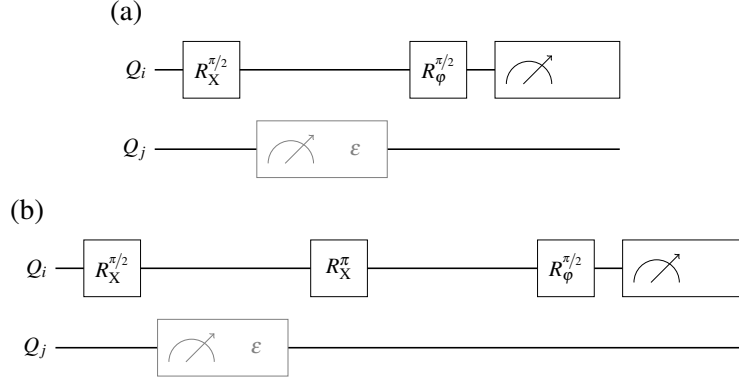
Figure 7.15: Circuit representation of the possible measurement induced cross-dephasing measurements. (a) Ramsey-type and (b) Echo-type measurement on Q_i with additional dephasing induced by (partial) measurement of Q_j with drive strength ε. The case $i = j$ was used for the quantum-efficiency measurements.
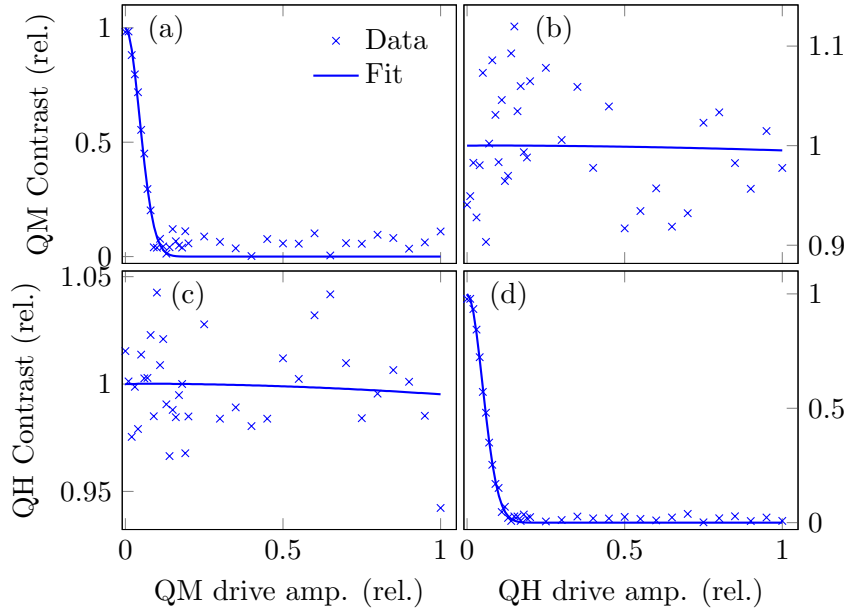

Figure 7.16: Matrix of the four coherence measurements. (a,d) Decohering effect of readout targeting QM and QH respectively as a function of its readout drive amplitude. (b,c) Cross-dephasing effect of the readout of QH and QM on QM and QL, respectively.

8 Conclusion and Outlook

In this work, we review the surface code theory and its requirements on gates and readout [1]. A technique to estimate the readout time and induced crosstalk on untargeted qubits is presented and used to optimize the frequencies and couplings of the readout resonators (RRs) and Purcell filter resonators (PFs). As a result of these simulations, a higher RR-qubit coupling is desired. The Starmon qubit design [43] is altered to implement this. As a side product, the bus connection scheme of the surface code needs to be altered, ensuring compatibility with the currently used connection port positions. Furthermore, implementation of microwave parameters, namely couplings and frequencies, is discussed. All this is then used to design and fabricate a three-qubit subset of surface 7 to examine both, the theoretical prediction of the readout process as well as the targeting of the microwave parameters. The device is then cooled down to conduct the characterization.

All resonator frequencies are found to be approximately 200 MHz below target. We attribute this to inaccuracies in the prediction of phase velocity and characteristic impedance, which was derived from the room-temperature resistivity, critical temperature and thickness of the film forming the resonators. With the limited data this chip provides, experimental determination of these parameters is not reliably possible. An more systematic experimental investigation of these parameters, as proposed in App. D, might allow more accurate predictions in the future.

Couplings between the resonators are measured to be much higher, while couplings towards the feedline are smaller than targeted. This is not consistently explained at this point. Further understanding might be obtained by using equivalent circuit diagram or finite-element high frequency simulations to calculate the feedline transmission, as outlined in [45].

The qubits sweetspot frequencies are above target, but the operation frequencies can be changed by means of applying a flux current to match the design for QM and QH, but unfortunately not for QL due to a connectivity issue in the wiring. We assume that full characterization of this qubit will be possible in future cooldowns. The anharmonicity and couplings of the qubit towards the RR and the bus connectors are well on target. This verifies the procedures used alter the qubits. The off-target sweetspot frequency can be attributed to a faulty machine used for the Josephson junction deposition.

At their target frequencies, energy relaxation times of 20 and $15\,\mu$s for QM and QH, respectively, were recorded. Measurement of the coherence time over a range of qubit frequencies reveals a good correspondence with the theoretical predictions of the Purcell rate. At target, the qubit energy relaxation times are clearly not limited by Purcell decay.

Despite these deviations, state-of-the art readout fidelities of >98% within 450 ns are demonstrated. Usage of parametric amplification is expected to allow for >99% readout fidelity within approximately 150 ns, which could be verified together with the characterization of QL. Recordings of the photon fields during readout can be consistently matched with the theoretical model used for predicting the duration of the readout process. This verifies the applicability of the methods used to

optimize the frequencies and couplings for readout.

At this time, only an upper measurement induced dephasing time bound of $T_2^{\mathrm{cr}} = 200\,\mu\mathrm{s}$ could be determined. We attribute this mainly to a low contrast of the measurement due to low coherence times far from the sweetspot. Using larger readout amplitude to increase the signal would not provide a systemic result. This is due to the fact, that the drive strength had previously been optimized to operate at the upper limit of the linear regime, required for the measurement. As such, this result does not allow confirmation of the simulated values. However, since the photon field predictions for the readout process are very accurate, we believe it likely that the prediction of crosstalk, based on the same photon fields, are also accurate. Furthermore, the absence of parametric amplification requires a higher photon number and therefore causes more dephasing than assumed in the simulations. Consequentially, the bound found here, can be assumed to be effectively lower when performing readout with parametric amplification. A similar argument can be made, when the same bound on crosstalk between QL and QM, which is predicted to be higher, is established. Ultimately however, higher coherence times would be required to increase contrast and provide the necessary time window for a measurement with repeated intermediate measurements, which would increase the total dephasing attainable in the linear regime. A device identical to the one presented here but with the desired sweetspot frequencies could provide coherence times of $T_2^{echo} \approx 2T_1$, which is $5 \sim 12$ times longer than in the device presented here.

These results show that this application of Purcell filtering can enable fast readout for the surface code, without limiting the qubit lifetime. Furthermore, simulations indicate and measurements hint at a reduction in measurement-induced cross-dephasing, allowing for the scaling required for surface code. As exemplified for S17 in Fig. 8.1, addition of the filters is possible in the current chip design of the surface code.
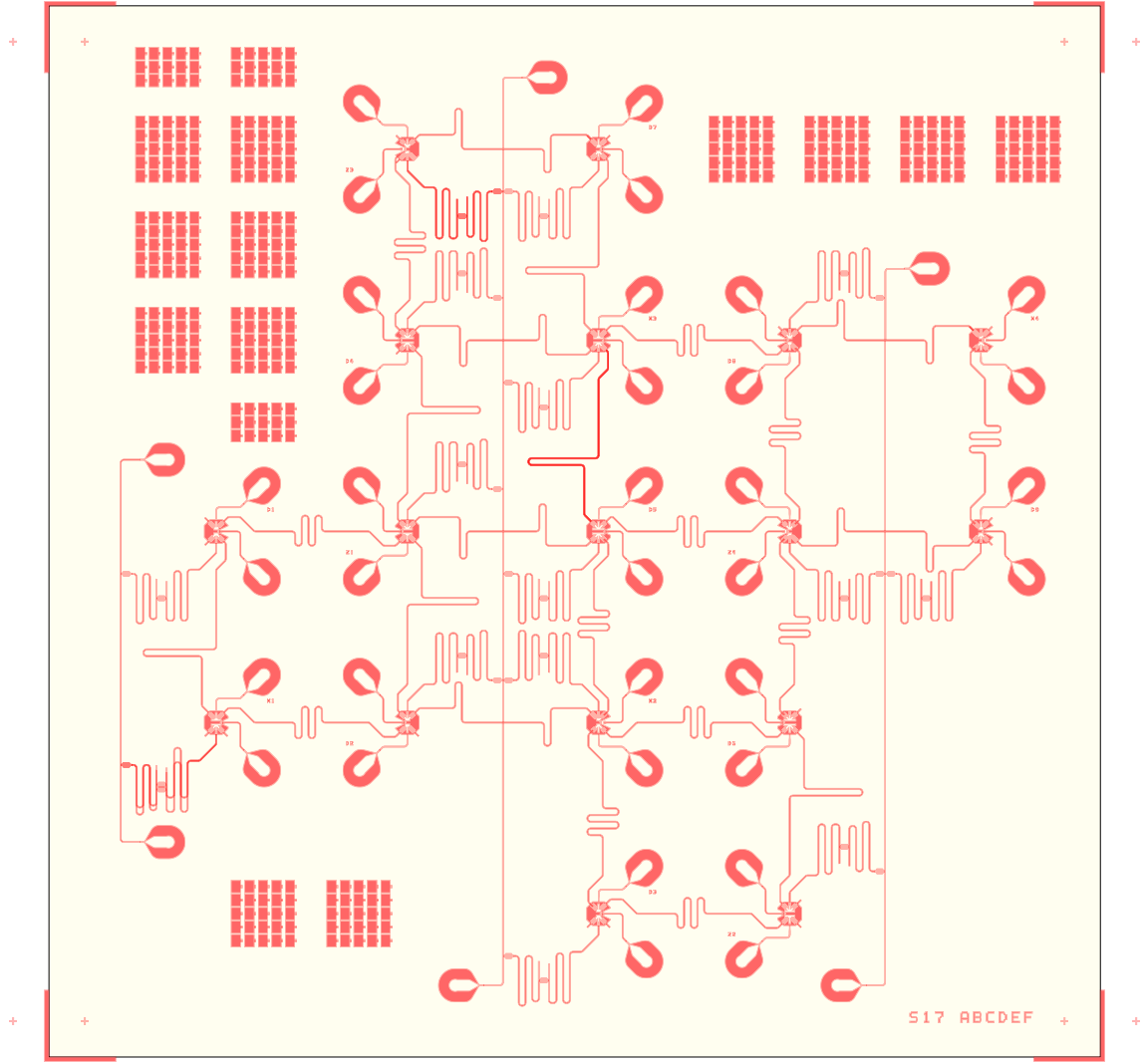
Figure 8.1: A sketch of the etch layer of a S17 chip with Purcell filtering. Based on and with the same TSV locations as the current design [45]. Note, how one of the ancilla qubit busses are rotated with respect to the others, as introduced in Sec. 5.2.

9   Acknowledgements

"Gratitude turns disappointment into lessons learned, discoveries made,
alternatives explored, and new plans set in motion."

— Auliq Ice

First, I want to first express my gratitude towards Leonardo Di Carlo for the opportunity to conduct research in a competitive and inspiring group. He kept challenging assumptions and driving for perfection.

However, without my daily supervisor, Niels Bultink, this research would not have been possible. Therefore, I want to express my profound gratitude for his patience and efficiency and providing insight and intuition. He always had an open ear for me and supported me throughout the thesis. I want to especially acknowledge his help in taking measurement data.

A very special acknowledgement and deep gratitude to Nandini Muthusubramanian, who spend nights and weekends in the cleanroom to fabricate the chip. I furthermore acknowledge Alessandro Bruno's contributions to the realization of the chip. This includes constantly pushing the envelop on fabrication recipes, supervising the cleanroom work, providing valuable input for the chip layout and helping in the final assembly of the device.

A very special thanks goes to Marc Beekman for countless valuable discussions as well as help with microwave simulations and his software package PyQIP. Through the chip design in general and the surface code in particular, our Master's theses had quite some overlap. It was delightful to explore the world of error-correction in superconducting qubits with him. Furthermore, I am grateful for all his comments on this thesis. For helping my understanding of microwave design, I want to acknowledge Nadia Haider and Stefano Poletto. Nadia Haider also pioneered the starmon qubit design and helped with the adaptation for this work. Brian Tarasinski helped with patient explanations and discussion of the differential equations for the simulation of the readout process. I would also like to thank Ramiro Sagastizabal for helpful discussions on two-qubit gates. My gratitude also goes to everyone involved in developing the control electronics in our lab, especially Jules van Oven, Jacob de Sterke and Xian Fu.

Lastly, I want to thank a few people on a more personal note. Adriaan Rol for taking the time to give me insights into his experiments and have discussions about coding style. Christian Dickel for discussing crazy ideas and his contribution to morale with his caustic humour. David Michalak for showing interest in my work and interesting discussions. I also want to express my gratitude to everyone, who supported me and helped me up when I most needed it. This includes Isabell Trinh and Ina Vollmer, but also many people from the group. The cohesion and support in the group was a valuable resource for this project.

References

[1] R. Versluis, S. Poletto, N. Khammassi, B. Tarasinski, N. Haider, D. Michalak, A. Bruno, K. Bertels, and L. DiCarlo, "Scalable Quantum Circuit and Control for a Superconducting Surface Code," *Phys. Rev. Applied*, vol. 8, no. 3, p. 034021, Sep. 2017. [Online]. Available: https://link.aps.org/doi/10.1103/PhysRevApplied.8.034021

[2] R. P. Feynman, "Simulating physics with computers," *International journal of theoretical physics*, vol. 21, no. 6, pp. 467–488, 1982. [Online]. Available: http://www.springerlink.com/index/t2x8115127841630.pdf

[3] S. Lloyd, "Universal Quantum Simulators," *Science*, vol. 273, no. 5278, pp. 1073–1078, Aug. 1996. [Online]. Available: http://www.sciencemag.org/cgi/doi/10.1126/science.273.5278.1073

[4] D. W. Berry, A. M. Childs, R. Cleve, R. Kothari, and R. D. Somma, "Exponential Improvement in Precision for Simulating Sparse Hamiltonians," in *Proceedings of the Forty-sixth Annual ACM Symposium on Theory of Computing*, ser. STOC '14. New York, NY, USA: ACM, 2014, pp. 283–292. [Online]. Available: http://doi.acm.org/10.1145/2591796.2591854

[5] P. W. Shor, "Algorithms for quantum computation: discrete logarithms and factoring," in *Proceedings 35th Annual Symposium on Foundations of Computer Science*, Nov. 1994, pp. 124–134.

[6] D. P. DiVincenzo, "The Physical Implementation of Quantum Computation," *Fortschritte der Physik*, vol. 48, no. 9-11, pp. 771–783, Oct. 2000. [Online]. Available: https://onlinelibrary.wiley.com/doi/abs/10.1002/1521-3978%28200009%2948%3A9/11%3C771%3A%3AAID-PROP771%3E3.0.CO%3B2-E

[7] P. W. Shor, "Scheme for reducing decoherence in quantum computer memory," *Phys. Rev. A*, vol. 52, no. 4, pp. R2493–R2496, Oct. 1995. [Online]. Available: https://link.aps.org/doi/10.1103/PhysRevA.52.R2493

[8] E. Knill, R. Laflamme, and W. Zurek, "Threshold Accuracy for Quantum Computation," *arXiv:quant-ph/9610011*, Oct. 1996, arXiv: quant-ph/9610011. [Online]. Available: http://arxiv.org/abs/quant-ph/9610011

[9] D. Aharonov and M. Ben-Or, "Fault Tolerant Quantum Computation with Constant Error," *arXiv:quant-ph/9611025*, Nov. 1996, arXiv: quant-ph/9611025. [Online]. Available: http://arxiv.org/abs/quant-ph/9611025

[10] J. Koch, T. M. Yu, J. Gambetta, A. A. Houck, D. I. Schuster, J. Majer, A. Blais, M. H. Devoret, S. M. Girvin, and R. J. Schoelkopf, "Charge-insensitive qubit design derived from the Cooper pair box," *Phys. Rev. A*, vol. 76, no. 4, p. 042319, Oct. 2007. [Online]. Available: https://link.aps.org/doi/10.1103/PhysRevA.76.042319

[11] E. A. Sete, A. Galiautdinov, E. Mlinar, J. M. Martinis, and A. N. Korotkov, "Catch-Disperse-Release Readout for Superconducting Qubits," *Physical Review Letters*, vol. 110, no. 21, May 2013. [Online]. Available: https://link.aps.org/doi/10.1103/PhysRevLett.110.210501

[12] M. D. Reed, B. R. Johnson, A. A. Houck, L. DiCarlo, J. M. Chow, D. I. Schuster, L. Frunzio, and R. J. Schoelkopf, "Fast reset and suppressing spontaneous emission of a superconducting qubit," *Applied Physics Letters*, vol. 96, no. 20, p. 203110, May 2010. [Online]. Available: http://aip.scitation.org/doi/10.1063/1.3435463

[13] E. Jeffrey, D. Sank, J. Mutus, T. White, J. Kelly, R. Barends, Y. Chen, Z. Chen, B. Chiaro, A. Dunsworth, A. Megrant, P. O'Malley, C. Neill, P. Roushan, A. Vainsencher, J. Wenner, A. Cleland, and J. M. Martinis, "Fast Accurate State Measurement with Superconducting Qubits," *Physical Review Letters*, vol. 112, no. 19, May 2014. [Online]. Available: https://link.aps.org/doi/10.1103/PhysRevLett.112.190504

[14] N. T. Bronn, Y. Liu, J. B. Hertzberg, A. D. Córcoles, A. A. Houck, J. M. Gambetta, and J. M. Chow, "Broadband filters for abatement of spontaneous emission in circuit quantum electrodynamics," *Applied Physics Letters*, vol. 107, no. 17, p. 172601, Oct. 2015. [Online]. Available: http://aip.scitation.org/doi/10.1063/1.4934867

[15] N. T. Bronn, E. Magesan, N. A. Masluk, J. M. Chow, J. M. Gambetta, and M. Steffen, "Reducing Spontaneous Emission in Circuit Quantum Electrodynamics by a Combined Readout/Filter Technique," *IEEE Transactions on Applied Superconductivity*, vol. 25, no. 5, pp. 1–10, Oct. 2015.

[16] A. G. Fowler, D. S. Wang, and L. C. L. Hollenberg, "Surface Code Quantum Error Correction Incorporating Accurate Error Propagation," *Quantum Info. Comput.*, vol. 11, no. 1, pp. 8–18, Jan. 2011. [Online]. Available: http://dl.acm.org/citation.cfm?id=2011383.2011385

[17] A. G. Fowler, M. Mariantoni, J. M. Martinis, and A. N. Cleland, "Surface codes: Towards practical large-scale quantum computation," *Physical Review A*, vol. 86, no. 3, Sep. 2012. [Online]. Available: https://link.aps.org/doi/10.1103/PhysRevA.86.032324

[18] T. E. O'Brien, B. Tarasinski, and L. DiCarlo, "Density-matrix simulation of small surface codes under current and projected experimental noise," *npj Quantum Information*, vol. 3, no. 1, Dec. 2017, arXiv: 1703.04136. [Online]. Available: http://arxiv.org/abs/1703.04136

[19] J. M. Martinis, "Course 13 Superconducting qubits and the physics of Josephson junctions," in *Les Houches*. Elsevier, 2004, vol. 79, pp. 487–520. [Online]. Available: http://linkinghub.elsevier.com/retrieve/pii/S0924809903800379

[20] R. C. Jaklevic, J. Lambe, A. H. Silver, and J. E. Mercereau, "Quantum Interference Effects in Josephson Tunneling," *Physical Review Letters*, vol. 12, no. 7, pp. 159–160, Feb. 1964. [Online]. Available: https://link.aps.org/doi/10.1103/PhysRevLett.12.159

[21] Y. Makhlin, G. Schön, and A. Shnirman, "Quantum-state engineering with Josephson-junction devices," *Rev. Mod. Phys.*, vol. 73, no. 2, pp. 357–400, May 2001. [Online]. Available: https://link.aps.org/doi/10.1103/RevModPhys.73.357

[22] F. Motzoi, J. M. Gambetta, P. Rebentrost, and F. K. Wilhelm, "Simple Pulses for Elimination of Leakage in Weakly Nonlinear Qubits," *Physical Review Letters*, vol. 103, no. 11, Sep. 2009. [Online]. Available: https://link.aps.org/doi/10.1103/PhysRevLett.103.110501

[23] L. DiCarlo, "Quantum computing with circuit QED," QDev-NBIA Summer School Copenhagen, Jul. 2016.

[24] A. Blais, R.-S. Huang, A. Wallraff, S. M. Girvin, and R. J. Schoelkopf, "Cavity quantum electrodynamics for superconducting electrical circuits: An architecture for quantum computation," *Phys. Rev. A*, vol. 69, no. 6, p. 062320, Jun. 2004. [Online]. Available: https://link.aps.org/doi/10.1103/PhysRevA.69.062320

[25] A. Wallraff, D. I. Schuster, A. Blais, L. Frunzio, R.-S. Huang, J. Majer, S. Kumar, S. M. Girvin, and R. J. Schoelkopf, "Strong coupling of a single photon to a superconducting qubit using circuit quantum electrodynamics," *Nature*, vol. 431, no. 7005, pp. 162–167, Sep. 2004. [Online]. Available: https://www-nature-com.tudelft.idm.oclc.org/articles/nature02851

[26] E. A. Sete, J. M. Martinis, and A. N. Korotkov, "Quantum theory of a bandpass Purcell filter for qubit readout," *Physical Review A*, vol. 92, no. 1, p. 012325, 2015. [Online]. Available: https://journals.aps.org/pra/abstract/10.1103/PhysRevA.92.012325

[27] T. Walter, P. Kurpiers, S. Gasparinetti, P. Magnard, A. Potočnik, Y. Salathé, M. Pechal, M. Mondal, M. Oppliger, C. Eichler, and A. Wallraff, "Rapid High-Fidelity Single-Shot Dispersive Readout of Superconducting Qubits," *Physical Review Applied*, vol. 7, no. 5, May 2017. [Online]. Available: http://link.aps.org/doi/10.1103/PhysRevApplied.7.054020

[28] D. F. Walls and G. J. Milburn, *Quantum Optics*, 2nd ed. Berlin Heidelberg: Springer-Verlag, 2008. [Online]. Available: //www.springer.com/gp/book/9783540285731

[29] J. Gambetta, A. Blais, D. I. Schuster, A. Wallraff, L. Frunzio, J. Majer, M. H. Devoret, S. M. Girvin, and R. J. Schoelkopf, "Qubit-photon interactions in a cavity: Measurement-induced dephasing and number splitting," *Physical Review A*, vol. 74, no. 4, Oct. 2006. [Online]. Available: https://journals.aps.org/pra/abstract/10.1103/PhysRevA.74.042318

[30] A. Frisk Kockum, L. Tornberg, and G. Johansson, "Undoing measurement-induced dephasing in circuit QED," *Phys. Rev. A*, vol. 85, no. 5, p. 052318, May 2012. [Online]. Available: https://link.aps.org/doi/10.1103/PhysRevA.85.052318

[31] J. Heinsoo, C. K. Andersen, A. Remm, S. Krinner, T. Walter, Y. Salathé, S. Gasperinetti, J.-C. Besse, A. Potočnik, C. Eichler, and A. Wallraff, "Rapid high-fidelity multiplexed readout of superconducting qubits," *arXiv:1801.07904 [quant-ph]*, Jan. 2018, arXiv: 1801.07904. [Online]. Available: http://arxiv.org/abs/1801.07904

[32] C. C. Bultink, B. Tarasinski, N. Haandbæk, S. Poletto, N. Haider, D. J. Michalak, A. Bruno, and L. DiCarlo, "General method for extracting the quantum efficiency of dispersive qubit readout in circuit QED," *Applied Physics Letters*, vol. 112, no. 9, p. 092601, Feb. 2018. [Online]. Available: http://aip.scitation.org/doi/10.1063/1.5015954

[33] C. A. Ryan, B. R. Johnson, J. M. Gambetta, J. M. Chow, M. P. da Silva, O. E. Dial, and T. A. Ohki, "Tomography via correlation of noisy measurement records," *Phys. Rev. A*, vol. 91, no. 2, p. 022118, Feb. 2015. [Online]. Available: https://link.aps.org/doi/10.1103/PhysRevA.91.022118

[34] E. Magesan, J. M. Gambetta, A. Córcoles, and J. M. Chow, "Machine Learning for Discriminating Quantum Measurement Trajectories and Improving Readout," *Phys. Rev. Lett.*, vol. 114, no. 20, p. 200501, May 2015. [Online]. Available: https://link.aps.org/doi/10.1103/PhysRevLett.114.200501

[35] D. M. Pozar, *Microwave engineering*. New Delhi: John Wiley & Sons, 2010, oCLC: 656349352.

[36] S. Gevorgian, L. Linner, and E. Kollberg, "CAD models for shielded multilayered CPW," *IEEE Transactions on Microwave Theory and Techniques*, vol. 43, no. 4, pp. 772–779, Apr. 1995. [Online]. Available: http://ieeexplore.ieee.org/document/375223/

[37] M. Göppl, A. Fragner, M. Baur, R. Bianchetti, S. Filipp, J. M. Fink, P. J. Leek, G. Puebla, L. Steffen, and A. Wallraff, "Coplanar waveguide resonators for circuit quantum electrodynamics," *Journal of Applied Physics*, vol. 104, no. 11, p. 113904, Dec. 2008. [Online]. Available: http://aip.scitation.org/doi/10.1063/1.3010859

[38] K. Watanabe, K. Yoshida, T. Aoki, and S. Kohjiro, "Kinetic Inductance of Superconducting Coplanar Waveguides," *Jpn. J. Appl. Phys.*, vol. 33, no. 10R, p. 5708, Oct. 1994. [Online]. Available: http://iopscience.iop.org/article/10.1143/JJAP.33.5708/meta

[39] B. A. Mazin, "Microwave kinetic inductance detectors," Ph.D. dissertation, TU Delft, Delft, Aug. 2004.

[40] J. Bourassa, F. Beaudoin, J. M. Gambetta, and A. Blais, "Josephson-junction-embedded transmission-line resonators: From Kerr medium to in-line transmon," *Physical Review A*, vol. 86, no. 1, Jul. 2012. [Online]. Available: https://link.aps.org/doi/10.1103/PhysRevA.86.013814

[41] C. C. Bultink, M. A. Rol, T. E. O'Brien, X. Fu, B. C. S. Dikken, C. Dickel, R. F. L. Vermeulen, J. C. de Sterke, A. Bruno, R. N. Schouten, and others, "Active resonator reset in the nonlinear dispersive regime of circuit QED," *Physical Review Applied*, vol. 6, no. 3, p. 034008, 2016. [Online]. Available: https://journals.aps.org/prapplied/abstract/10.1103/PhysRevApplied.6.034008

[42] C. C. Bultink, N. Haandbaek, L. DiCarlo, R. Sagastizabal, and M. A. Rol, "Multiplexed single-shot readout with real-time crosstalk," IARPA, Chicago, Jan. 2018.

[43] N. Haider *et al.*, "Design and analysis of superconducting qubits for extensible surface coding," (In preperation).

[44] R. W. Klopfenstein, "A Transmission Line Taper of Improved Design," *Proceedings of the IRE*, vol. 44, no. 1, pp. 31–35, Jan. 1956.

[45] M. W. Beekman, "Superconducting Multi-Qubit Chip Layout Optimization through Electromagnetic Analysis," Master's thesis, TU Delft, Delft, (In preperation).

[46] L. H. Gabrielli, "gdspy: Python module for creating GDSII stream files, usually CAD layouts," Jun. 2015. [Online]. Available: https://github.com/heitzmann/gdspy

[47] F. Yan, S. Gustavsson, A. Kamal, J. Birenbaum, A. P. Sears, D. Hover, T. J. Gudmundsen, D. Rosenberg, G. Samach, S. Weber, J. L. Yoder, T. P. Orlando, J. Clarke, A. J. Kerman, and W. D. Oliver, "The flux qubit revisited to enhance coherence and reproducibility," *Nature Communications*, vol. 7, p. 12964, Nov. 2016. [Online]. Available: https://www.nature.com/articles/ncomms12964

[48] D. Ristè, J. G. van Leeuwen, H.-S. Ku, K. W. Lehnert, and L. DiCarlo, "Initialization by Measurement of a Superconducting Quantum Bit Circuit," *Physical Review Letters*, vol. 109, no. 5, Aug. 2012. [Online]. Available: https://link.aps.org/doi/10.1103/PhysRevLett.109.050507

[49] T. C. White, J. Y. Mutus, I.-C. Hoi, R. Barends, B. Campbell, Y. Chen, Z. Chen, B. Chiaro, A. Dunsworth, E. Jeffrey, J. Kelly, A. Megrant, C. Neill, P. J. J. O'Malley, P. Roushan, D. Sank, A. Vainsencher, J. Wenner, S. Chaudhuri, J. Gao, and J. M. Martinis, "Traveling wave parametric amplifier with Josephson junctions using minimal resonator phase matching," *Appl. Phys. Lett.*, vol. 106, no. 24, p. 242601, Jun. 2015. [Online]. Available: https://aip.scitation.org/doi/abs/10.1063/1.4922348

[50] S. Asaad, "Exploring frequency re-use with transmon qubits in a cQED architecture," Master's thesis, TU Delft, Delft, Jun. 2015.

List of Figures

Appendix A   CPW capacitance Simulations

Here we show the procedure used to estimate the capacitance per unit length using the *CST EM Studio* low-frequency finite-element simulations software. The simulation setup can be seen in Fig. A.1; it consists of a substrate block, which in out case is Silicon with a dielectric constant ε and a thickness of d. On this, five blocks of superconducting film of thickness t are placed. Two of these are representing the ground planes on each side of the CPW with a gap g to the central conductor of width w, which is divided into three parts with small interruptions (gaps) smaller than the height of the film. The two outer, electrically separated pieces remove the effect of the fringing field on the test piece in the middle.
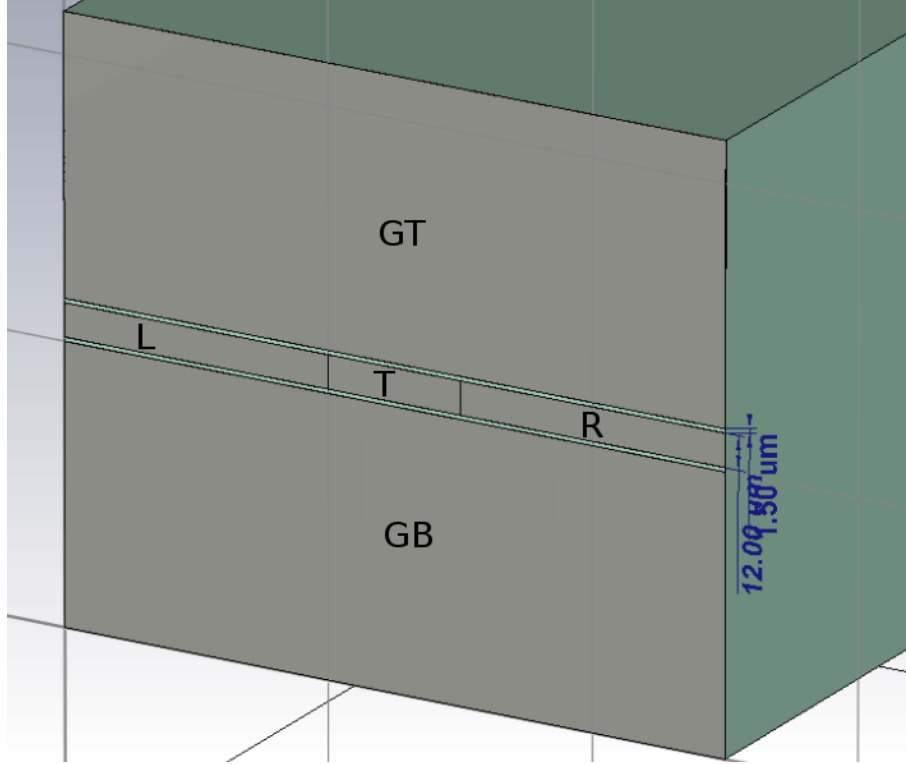

Figure A.1: Screenshot of the simulation setup for determining the capacitance per unit length with text-overlay. The green block represents the substrate, while the gray ones represent the film. There are five pieces of film: two ground planes in the top (GT) and bottom (GB) the test-CPW (T) and two dummy-pieces (L and R) to remove the effect of fringing fields.

Varying the length of the central conductor piece and performing linear regression over the calculated capacity of it to the ground plane allows precise extraction of C_l, see Fig. A.3. Varying the gap g as well, to fit C_l as a function of g. Here a fit function $C_l(g) = a \cdot \ln(g) + b + c \cdot \sqrt{g}$ where g is given in metres has been used. While the first two terms have clear correlation to analytical geometric expression in Ch. 4.1, the last term is only motivated by the observation that it improves the fitting result.

Application of the outlined method with a fixed width of $w = 12\,\mu$m, $d = 520\,\mu$m, $\varepsilon = 11.45$ (dielectric constant of Silicon at cryogenic temperatures) and $t = 200$ nm we extract $a = -8.1568 \cdot 10^{-11}$F/m, $b = -8.6833 \cdot 10^{-10}$F/m and $c = 2.4010 \cdot 10^{-8}$F/m with $(1 - R^2) = 4.1 \cdot 10^{-5}$. These results can be seen in Fig. A.2, together with the result of the analytical expression from Ch. 4.1

with

$$\varepsilon_{\text{eff}} = \varepsilon - \frac{0.7 \cdot (\varepsilon - 1) \cdot t}{g \cdot K(k_0)/K(k_0') + 0.7 \cdot t}.$$
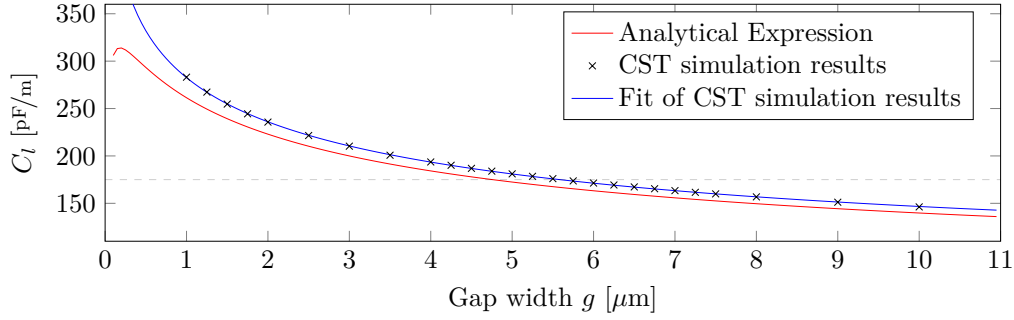

Figure A.2: Plot of the extracted capacitance per unit length values (crosses), a logarithmic fit to that data (red) and the currently used analytical expression (blue).

Although the simulation seems to be very close to the analytical solution, it can be seen that in order to achieve an capacitance $C_l = 175\,\text{pF/m}$ we would chose a gap of $\sim 4.8\,\mu\text{m}$ according to the analytical solution, where the simulation results suggest $\sim 5.6\,\mu\text{m}$ (see grey dashed line in Fig. A.2), which can lead to differences of more than 2% in phase velocity and characteristic impedance. This would mean a targeting inaccuracy of 140 MHz at 7 GHz.

It can furthermore be noted, that this difference between analytical and simulated capacitance is much larger than the difference between $t = 150\,\text{nm}$ and $200\,\text{nm}$. Therefore, these simulations were not repeated for the 250 nm thick film measured on the chip. However, the analytical expression for the inductance was used with the latter number.
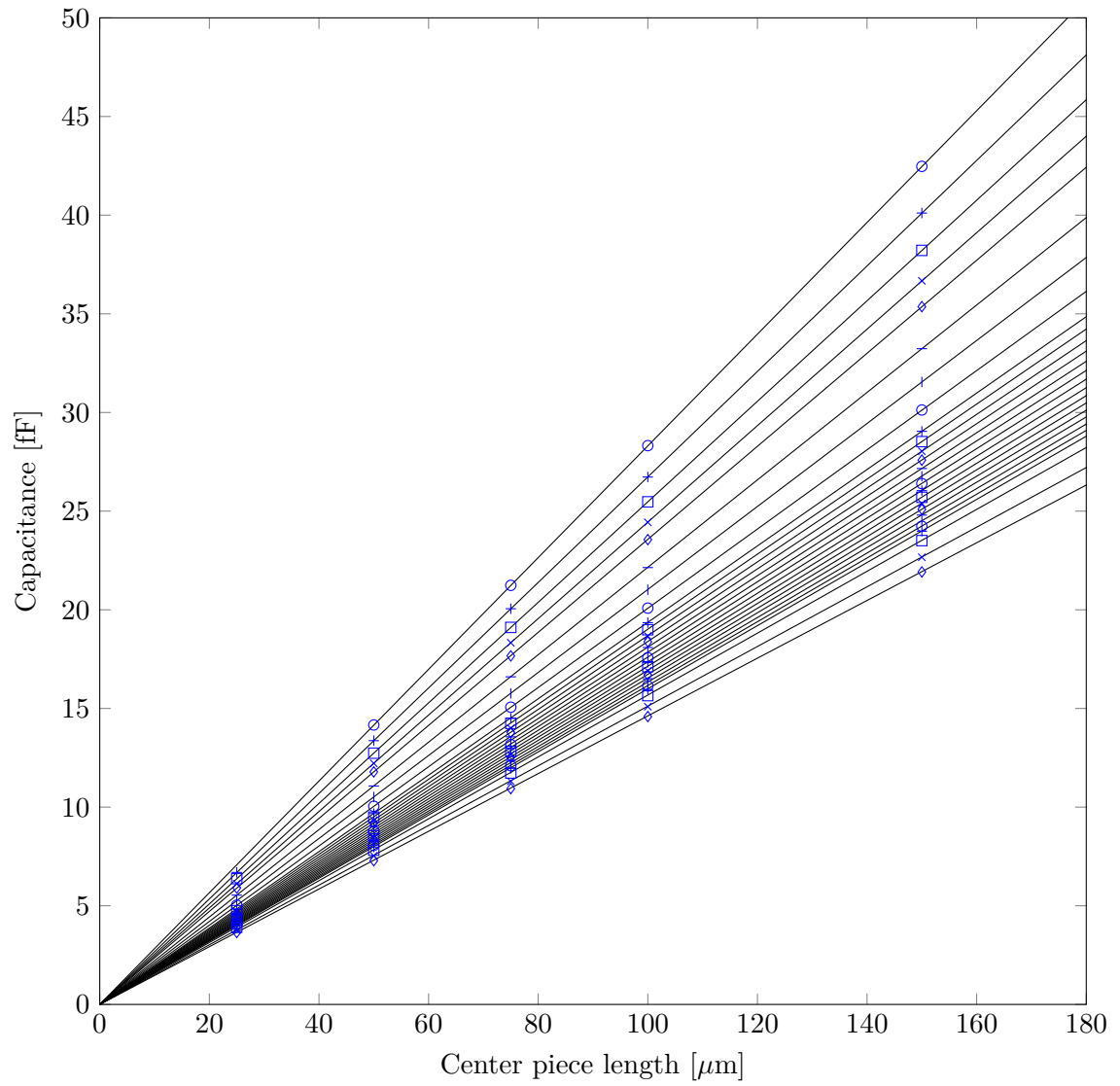
B

Figure A.3: Simulated (blue marker) capacitances of the CPW and fits (black lines), for gap widths of 1.0, 1.25, 1.5, 1.75, 2.0, 2.5, 3.0, 3.5, 4.0, 4.25, 4.5, 4.75, 5.0, 5.25, 5.5, 5.75, 6.0, 6.25, 6.5, 6.75, 7.0, 7.25, 7.5, 8.0, 9.0 and 10.0 μm (top to bottom).

Appendix B   Constraints for Equations of Motion

This section lists the constraints and dependencies, that have to be taken into account when simulating with the differential equations from chapter 3.

- The dispersive shift is not a free parameter - it highly depends on other parameters, as seen in Eq. (2.2)

$$\chi \simeq \frac{g^2}{\Delta_{qr}} \frac{\delta_\alpha}{\delta_\alpha + \Delta_{qr}}$$

- $\kappa_r = \frac{4|J|^2}{\kappa_f} \frac{1}{1 + [2(\omega_r - \omega_f / \kappa_f)]^2}$, which assumes $\kappa_f \ll J$ [26], alternatively

  $\kappa_r = \frac{1}{2} \left(\kappa_f - \Re \left(\sqrt{-16J^2 + (\kappa_f - 2j\Delta_{fd})^2} \right) \right)$ can be used without that restriction [31]

- If the dispersive shift becomes too large, the risk of exciting higher states becomes seizable, so we should restrict ourselves to $\chi < \delta_\alpha$ and $\delta_\alpha \ll |\Delta_{qr}|$ [26]

- For the dispersive shift to remain valid, $1 \ll n_{crit} = \left| \frac{\Delta_{qr}}{4g} \right|^2$ needs to be fulfilled [26]

- $g < \min(|\Delta_{qr} + \delta_\alpha|, |\Delta_{qr} - \delta_\alpha|)$ and $g \ll |\Delta_{qr}|$

- The Pucell rate according to Eq. (2.4) should remain below target

Appendix C   Interdigitated Capacitor Simulations

Using a similar setup as in CPW capacitance Simulations, the capacitance matrices of interdigitated capacitors were determined. The results in Fig. C.2 show, that the capacitances are very linear in the length of the fingers l_{fi}. Thus, this length was varied and linear regression performed on it for different gaps $s_f = g_f$, using the name convention established in Fig. C.1. All non-varied parameters are listed in Tab. C.1 with the used value. These results allow to directly predict the to-ground capacitances and finger length, given a gap and main capacitance value.
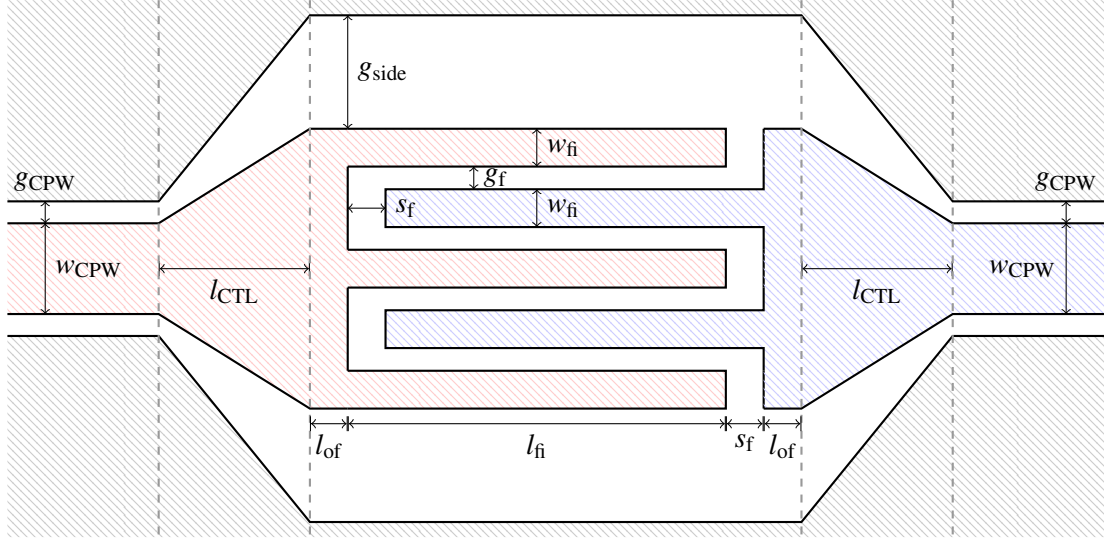

Figure C.1: Visualization of the dimensional parameters of the interdigitated capacitor, here overlaid on the example of a $n_f = 3 + 2$ finger model. The gray dashed lines are only for visual reference. *Main* refers to the capacitance between the red and green, *Ground 1* between red and grey and *Ground 2* between the blue and grey hatched areas. All hatched areas are covered with film, while the white area is exposed substrate.

Table C.1: Shared parameters of the interdigitated capacitors simulated in this appendix.

Parameter	Value	Unit
n_f	5+4	
w_{fi}	4	μm
l_{CTL}	30	μm
l_{of}	5	μm
w_{CPW}	12	μm
g_{CPW}	6	μm
t_{sub}	520	μm
g_{side}	20	μm

In order to generalize the results, the fitted parameters are then fitted a second time with a polygon of second order. The results of this fit can be found in Tab. C.2. With this result, the previous calculations can be done with any gap width between $3 - 6\,\mu$m.

E

Table C.2: The fitted results from fitting the linear capacitance fits using $a \cdot (g_f)^2 + b \cdot g_f + c$. All numbers are in units of Farads and metres.

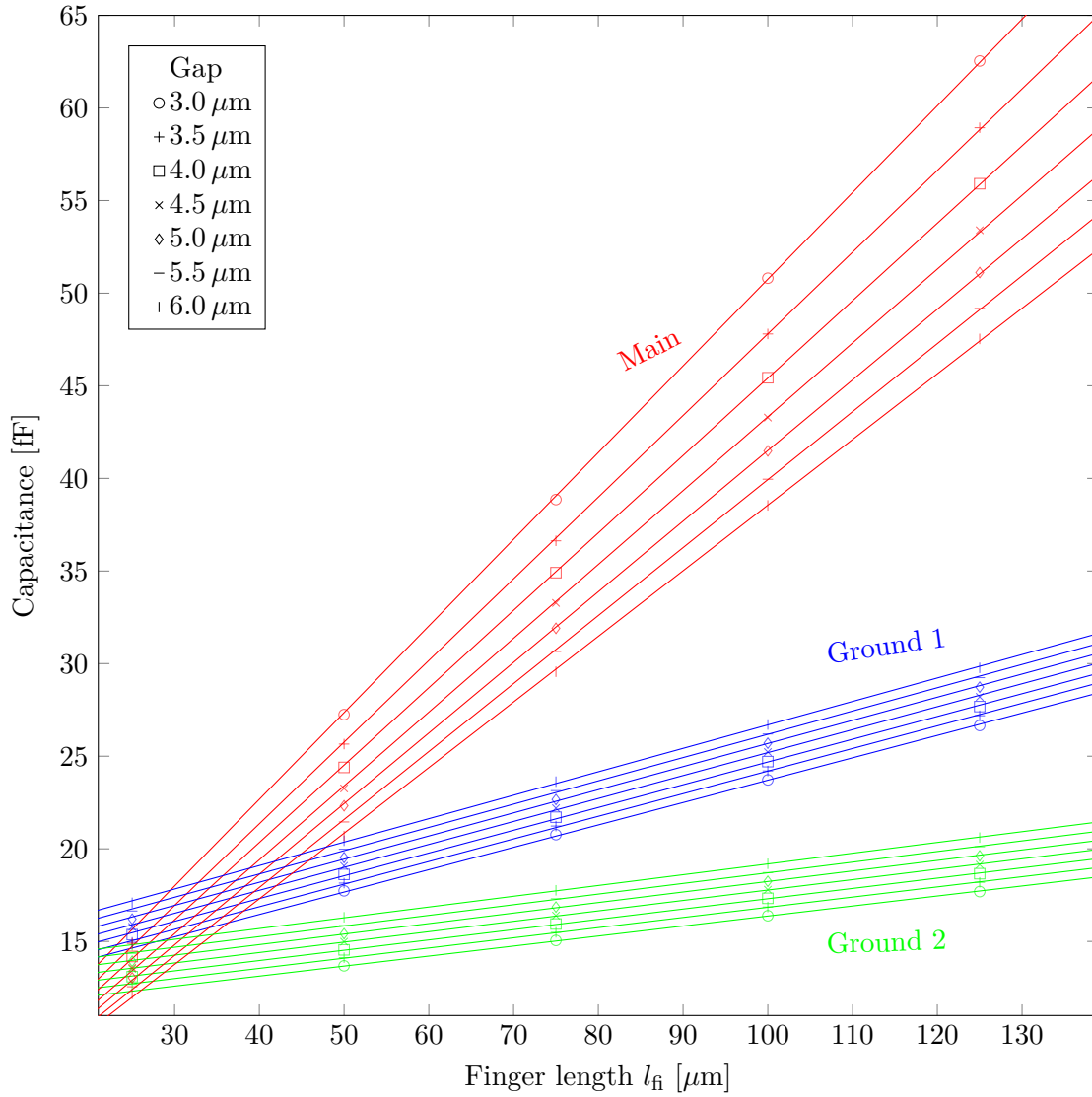| Fit	a	b	c
Main Capacitance Slope	$+5.687$	$-8.873 \cdot 10^{-5}$	$+6.824 \cdot 10^{-10}$
Main Capacitance Intercept	$+2.590 \cdot 10^{-5}$	$-4.952 \cdot 10^{-10}$	$+5.176 \cdot 10^{-15}$
Ground 1 Capacitance Slope	$-8.859 \cdot 10^{-2}$	$+2.693 \cdot 10^{-6}$	$+1.136 \cdot 10^{-10}$
Ground 1 Capacitance Intercept	$+1.251 \cdot 10^{-5}$	$+6.926 \cdot 10^{-10}$	$+9.425 \cdot 10^{-15}$
Ground 2 Capacitance Slope	$-5.834 \cdot 10^{-2}$	$+1.830 \cdot 10^{-6}$	$+4.917 \cdot 10^{-11}$
Ground 2 Capacitance Intercept	$+8.227 \cdot 10^{-6}$	$+7.300 \cdot 10^{-10}$	$+8.696 \cdot 10^{-15}$

Figure C.2: Capacitances of the interdigitated capacitor as extracted from CST, overlaid with linear fits. The colours note the capacitance type and the symbol the gap width (see main text).

Appendix D   Notes on Phase Velocity

As seen in the measurement results, the phase velocity and the capacitance values should be well known to achieve accurate targeting. Here we propose a simple measurement setup to determine these values.

The frequency of a quarter-wave resonator coupled to a feedline is dependent on the coupling capacity C_C, the phase velocity v, the length of the resonator and its characteristic impedance, as seen in Eq. (4.8). As seen in Interdigitated Capacitor Simulations, it can very accurately be assumed that the capacitance of an interdigitated capacitor is linear in the length of the fingers if all other parameters are fixed. Due to the fact, that lengths are very accurately controllable in micro-fabrication, there is only a total of four unknown parameters left: v, Z_l as well as the slope and intercept of the capacitance. We propose not to use a range of resonators with varying length, coupled by interdigitated capacitors to the feedline with a range of finger lengths. With enough data points, this would allows us to fit the frequency measurements and thus determine the four free parameters. Fitting the linewidths would allow for dissection of the capacitance parameters into main to-ground capacitance values. A layout for such a measurement can be seen in Fig. D.1. Fast measurement can be performed at 300 mK, which has been shown to yield very similar results to the ~ 10 mK used for the qubit chips [50].
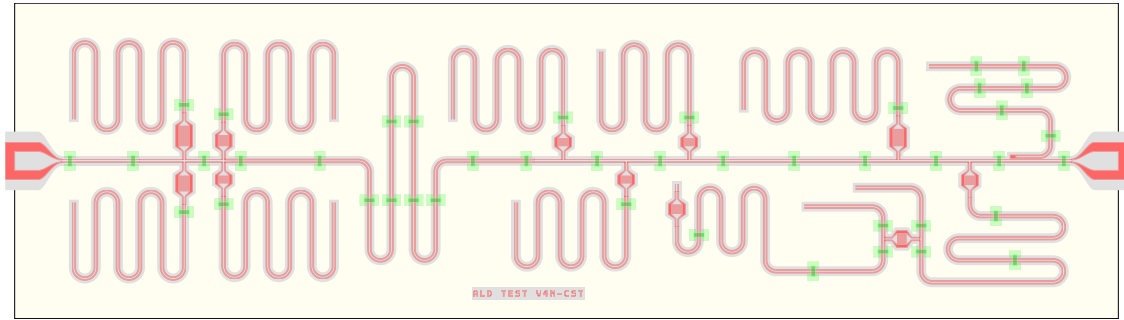

Figure D.1: Rendering of the chip layout (excluding the holy ground layer) to determine the phase velocity, characteristic impedance as well as coupling capacitor slope and intercept.

The knowledge of the phase velocity and characteristic impedance of a CPW geometry as well as the behaviour of the capacitances in a given film would allow for very precise resonator frequency and coupling targeting. Systematically taking these measurements with a range of different films, would allow to apply corrections to the known formulas for these properties.

Appendix E   Fabrication Details

Base-Layer

A high resistivity N-type silicon wafer (Topsil) of diameter 100 mm and thickness 525 μm was cleaned with acetone and isopropanol (IPA). The wafer was then immersed in hydrofluric acid for two minutes and rinsed with H_2O to remove residual oxides. The cleaned wafer was sputtered with a 250 nm niobium titanium nitride (NbTiN) layer. The sheet resistance of the wafer was measured using the four-probe method and the critical temperature of the sputtered film of NbTiN was determined. These input parameters were used to determine the phase velocity of the film.

The NbTiN wafer was coated with a protective layer of photoresist and diced into smaller tiles of dimensions 15×20 mm. With the size of the designed device, three replicates were patterned per tile. For patterning the base layer of the device, the sample tile was cleaned of debris from dicing and stripped of photoresist using acetone and IPA followed by ultrasonication in fresh IPA for five minutes. Prior to spinning a new, clean layer of resist, the tile was baked for one minute at 110 °C on a hot plate. A high contrast positive tone electron-beam resist, namely AR-P 6200 series, (CSAR) was spun at 1000 rpm and baked for 120 s at 150 °C. Next, the device was patterning using an electon-beam (e-beam) with a dose of 340 $\mu C/cm^2$. The exposed base layer resist was developed using pentyl acetate (60 s), stopper O-xylene (10 s) and rinsed using IPA. The tile was transferred to a reactive ion etcher and the exposed NbTiN region was etched using a mixture of SF_6/O_2 and the residual resist was stripped using a hot solution of PRS-3000.

Josephson Junction deposition

For the JJ fabrication step, the base layer was first spun with a double-layer e-beam resist (PMGI SF-7 followed by PMMA 950K (3% in anisole)) at 2000 rpm. The PMGI resist was soft-baked at 110 °C for one minute followed by five minutes of baking at 175 °C whereas the PMMA resist was only baked at 175 °C for five minutes. To produce the overlapping Al-AlO$_x$-Al layers that form the JJ, rectangular windows were patterned and developed using a mixture of methyl isobutyl ketone (MIBK) and IPA in the ratio 1:3 for 60 s, followed by a stopper solution of 1:3 mixture of ethanol and IPA, final rinsing with IPA and dried under N_2. To develop the PMGI layer, the chip was rinsed in DI H_2O first and then developed using MF321 for 20 s followed by rinsing in H_2O again. To remove residual resist debris in the JJ pattern, the devices were subjected to O_2 ashing step for 45 s. Then, to remove the oxide layer, the chip was immersed in buffered oxide etch solution (BOE) diluted with 1:1 H_2O for 30 s. The chips were immediately blow-dried under N_2 and transferred to the shadow evaporator.

The shadow evaporator comprises a sample stage connected to three motors, with motor 1 used for translation along the y axis while motor 2 and 3 are used for rotational movement of the stage. The chips were transferred from the evaporator loadlock to the main chamber after the pressure decreased to 10^{-7} mbar. Prior to deposition of aluminum, about 30 nm of titanium was evaporated in order to decrease the pressure of the chamber to about $2 \cdot 10^{-8}$ mbar. For deposition of the bottom electrode of thickness 55 nm, the sample stage was rotated using motor 2 and 3 by

angles $-205°$ and $210°$, respectively, relative to its initial position. After deposition of the bottom electrode, the Al_2O_x tunnel barrier of thickness 2 nm was grown. The sample chamber was isolated from the target and purged with O_2 gas at pressure 0.7 mbar and the oxidation process was carried out for 666 s after which the oxygen was pumped out of the chamber. For deposition of the top electrode, the sample holder was rotated using motor 2 by an angle $540°$ relative to its position. The top electrode was deposited upto a final thickness of 110 nm. A final capping layer of Al_2O_x was grown using the same procedure as followed for the tunnel barrier. The chips were lifted off in a bath of N-methyl pyrrolidone (NMP) at 90 °C.

Post lift-off, the room-temperature resistance of the Josephson junctions were measured using a two-probe station using minimum illumination for the microscope. This resistance value allows prediction of E_J. By sweeping the junction width on test devices, the width of the pattern corresponding the target frequencies of the qubits were determined.

Airbridges

For the fabrication of airbridges, the chips were spun twice with the resist PMGI SF-15, consecutively at 2500 rpm and baked at $180°$ for five minutes. The first e-beam step for airbridges involves patterning side pads along the length of all CPW transmission lines on the device to allow grounding by the airbridges. The pads were written using an dose of $800 \mu C/cm^2$ and the pattern was developed using 1:4 ratio of AZ400K developer and DI H_2O. Post development, the PMGI SF-15 layer was subjected to reflow by heating the chip upto $200°$ for 180 s in order to obtain the smooth curved profile of the airbridges. Then, the chips were left in ambient conditions of the cleanroom overnight to allow for rehydration of the resist layer and minimise cracking of the resist during the second e-beam step. For the second e-beam step, a bilayer of MMA/MAA and PMMA was spun to pattern the bridges. First, MMA/MAA resist (8.5% in ethyl lactate 11) was spun at 1000 rpm followed by a ramped bake upto $150°$ for 120 s. This was followed by spinning PMMA 950K (8% in anisole) at 1500 rpm and baked at $150°$ for five minutes. The bridges were patterned using a dose of $1050 \mu C/cm^2$ such that the bridges overlap the side pads and was developed using 1:3 MIBK : IPA solution. For deposition of aluminum, the chips were transferred to an e-beam evaporator (Temescal) for deposition of 450 nm of Al. Prior to deposition step, the oxides on the exposed NbTiN regions were removed by argon ion milling for 60 s.

Finish and Wiring

After deposition of the airbridges, the chips were coated with photoresist (Microposit® S1813), baked for 60 s at $110°$ and prepared for dicing the devices from the tile using the DISCO dicer (DAD 3220). The diced devices were immersed in a bath of hot NMP solution and lifted-off gently in order to avoid breaking the airbridges. The lifted off devices were cleaned in fresh IPA, air-dried and packed in Gel-Pak® boxes. A final room-temperature resistance measurement of the JJs was carried out and the device with resistance values closest to the target qubit frequencies was chosen for measurements.

The copper printed circuit board (PCB) used for assembling the chip comprises 8 SMP ports with a central trench whose dimensions correspond to that of the fabricated device. The PCB was scrubbed using glass wool-tipped pen and ultrasonicated in IPA. Then the SMP connectors were soldered to the PCB using lead-tin solder and the chip was glued to the PCB using Apiezon-N wax.

Appendix F   Fitting Procedures

Filter-Resonator

In order to fit the feedline transmission, an extended version of Eq. (3.10) was used. Firstly internal losses γ_r and γ_f of the RR and PF, respectively, were taken into account as in [31]. Taking experimental circumstances into consideration we used

$$S_{21}(\omega) = A(\omega) \cdot \left(A_p - \frac{e^{-i\phi} \cdot \kappa_f(\gamma_r + 2i(\omega - \omega_r) + \kappa_r)}{4J^2 + (\gamma_f + 2i(\omega - \omega_f) + \kappa_f)(\gamma_r + 2i(\omega - \omega_r) + \kappa_r)} \right) \,, \tag{F.1}$$

where A_p is a arbitrary scaling factor and $A(\omega)$ a global amplitude, given by

$$A(\omega) = A_0 \cdot (1 - \Gamma(\omega)) \cdot \frac{1 + \alpha_s(\omega - \omega_{s,0})}{\omega_{s,0}} \cdot e^{-i(\phi_s \omega + \phi_{s,0})}$$

modelling the input-capacitor,

$$\Gamma(\omega) = {}^1\!/_{(1 + 2i\omega Z_0 C_{in})} \,,$$

slope α_s and offset $\omega_{s,0}$ of the amplification strength as a function of frequency and the phase-wrapping with constant ϕ_s and offset $\phi_{s,0}$ caused by the finite length of the fridge wiring.

   It should be noted, that these fits require very good initial guesses to converge. We would use a four-step procedure, applied iteratively is necessary:

1. Guessing the resonators frequencies as half the distance of the designed J from the centre of both minima. Inserting all other values as design values.

2. Fit $|S_{21}|$, as the phase wrapping term can be ignored here. Increasing and decreasing the guess for J (and the frequencies accordingly) until a reasonably good fit is obtained. This might also require to change the guess for some of the other parameters.

3. Fit the phase wrapping on a wide feedline scan, treating it as unperturbed by elements coupled to it, to obtain parameters ϕ_s and $\phi_{s,0}$.

4. Fit S_{21} with the parameters obtained from the previous steps as starting guess.

Flux Arch

$$\omega_q(I) = (\omega_{q,max} + E_C) \cdot \left(\alpha_a^2 + (1 - \alpha_a^2) \cdot \cos\left(\pi(I - I_0)/I_{\Phi_0} \right)^2 \right)^{1/4} - E_C \,, \tag{F.2}$$

where I is the flux current, a the dimensionless asymmetry given by $\alpha_a = \left| \frac{E_{J_1} - E_{J_2}}{E_{J_1} + E_{J_2}} \right|$, E_{J_1} and E_{J_2} are the Energies of the two JJs in the SQUID loop, I_{Φ_0} the current per flux, I_0 the flux offset.

Readout Fidelity

The number of shots for each prepared state are fitted with a two-dimensional Gaussian function to find the centre point. The data is then rotated along this axis and integrated along it, resulting in two graphs representing cumulative shots along an effective integration voltage V_{eff}. After normalization

to one, these are then fitted with the functions

$$g^{(|0\rangle)} = ((1 - p_{\text{sp}}^{(0)})f_{\text{CDF}}^{(|0\rangle)} + p_{\text{sp}}^{(0)}f_{\text{CDF}}^{(|1\rangle)}) \quad \text{and}$$

$$g^{(|1\rangle)} = ((1 - p_{\text{sp}}^{(1)})f_{\text{CDF}}^{(|1\rangle)} + p_{\text{sp}}^{(1)}f_{\text{CDF}}^{(|0\rangle)}) \quad , \text{where}$$

$$f_{\text{CDF}}^{(|0\rangle/|1\rangle)} = \frac{1}{2}\left[1 + \text{erf}\left(\frac{V_{\text{eff}}^{(0/1)} - V_{\text{eff},0}^{(0/1)}}{\sqrt{2}\sigma^{(0/1)}}\right)\right]$$

the Cumulative Distribution Function (CDF), $V_{\text{eff}}^{(0/1)}$ the effective integrated voltage, $V_{\text{eff},0}^{(0/1)}$ the centre of the associated Gaussian and $p_{\text{sp}}^{(0)}$ the part of the population found in the opposite state than prepared.

The Fidelity is the maximum distance between the two curves and the decision boundary the effective voltage V_{eff} of this point. An alternative approach is to create a histogram after rotation rather than integration. This can then be fitted by using the Gaussian associated with the CDF instead. This however will lead to some loss of information an thus accuracy. Note, that the results of the CDF fit can just as well be inserted into the Gaussian analogon to retrieve a more accurate fit of the more intuitive histograms. This procedure was used in Fig. 7.12.

Quantum efficiency

The same procedure as in [32] as used.

L